AD-784 857

THE EFFECTS OF MESO-SCALE AND SMALL-SCALE INTERACTIONS ON GLOBAL CLIMATE

T. N. Jerskey, et al

Systems, Science and Software

Prepared for:

Air Force Office of Scientific Research
Advanced Research Project Agency

15 July 1974

SECURITY CLASSIFICATION OF THIS PAGE (When Data Entered)

| REPORT DOCUMENTATION PAGE | | READ INSTRUCTIONS BEFORE COMPLETING FORM |
|---|---|---|
| 1. REPORT NUMBER<br>AFOSR - TR - 74 - 1338 | 2. GOVT ACCESSION NO. | 3. RECIPIENT'S CATALOG NUMBER<br>AD-784 857 |
| 4. TITLE (and Subtitle)<br>The Effects of Meso-Scale and Small-Scale Interactions on Global Climate | | 5. TYPE OF REPORT & PERIOD COVERED<br>Semiannual Technical Report<br>1 Nov. 1973 - 15 July 1974 |
| | | 6. PERFORMING ORG. REPORT NUMBER<br>SSS-R-74-2331 |
| 7. AUTHOR(s)<br>T.N. Jerskey<br>W.J. Wiscombe | | 8. CONTRACT OR GRANT NUMBER(s)<br>F44620-74-C-0035 |
| 9. PERFORMING ORGANIZATION NAME AND ADDRESS<br>Systems, Science and Software<br>P.O. Box 1620<br>La Jolla, California 92037 | | 10. PROGRAM ELEMENT, PROJECT, TASK AREA & WORK UNIT NUMBERS |
| 11. CONTROLLING OFFICE NAME AND ADDRESS<br>Defense Advanced Research Projects Agency<br>1400 Wilson Blvd.<br>Arlington, Virginia 22209 | | 12. REPORT DATE<br>15 July 1974 |
| | | 13. NUMBER OF PAGES<br>84 |
| 14. MONITORING AGENCY NAME & ADDRESS(if different from Controlling Office) | | 15. SECURITY CLASS. (of this report)<br>Unclassified |
| | | 15a. DECLASSIFICATION DOWNGRADING SCHEDULE |

16. DISTRIBUTION STATEMENT (of this Report)

17. DISTRIBUTION STATEMENT (of the abstract entered in Block 20, if different from Report)

18. SUPPLEMENTARY NOTES

19. KEY WORDS (Continue on reverse side if necessary and identify by block number)

lee waves
wave drag
radiation

20. ABSTRACT (Continue on reverse side if necessary and identify by block number)

During the past six months of the contract period considerable progress was made toward parameterization of the lee wave drag for incorporation into the Mintz-Arakawa Global Circulation Model. The limitations imposed by the two-level model are described in this report, and an analytic model consistent with the data available from the two-level model has been formulated for the zonal component of the stress. We have outlined the work to be completed to formulate the meridional stress.

DD 1 JAN 73 1473 EDITION OF 1 NOV 65 IS OBSOLETE

SECURITY CLASSIFICATION OF THIS PAGE (When Data Entered)

## 20. ABSTRACT

The work on the radiation portion of the contract has primarily involved the improvement of existing codes. The radiation codes have been made compatible with the IBM 360/91 computer facility at UCLA.

TABLE OF CONTENTS

TABLE OF CONTENTS (continued)

INTRODUCTION

Progress on the development of the wave drag codes and improvements in the radiation code were considerably slowed by the changeover to the UCLA 360/91 computing system. Our unfamiliarity with the new system, inadequate consulting services, and frequent shutdowns of our host (the UCSD computing center) contributed to long delays in our program plan. Most of the work which remains to be completed in this contract would have been accomplished during this report period if we had been operating on our local computing system.

At the close of the last contract period, the linear steady-state model had been formulated. The stress integral had been separated into an atmospheric response function and a topography spectrum function. All of the information about the atmosphere had been contained in the atmospheric response function, and all the information about the topography was contained in the topography spectrum function.

Our objective in this contract period has been to parameterize the drag induced by the mountain lee waves by characterizing the atmospheric response function in terms of the atmospheric variables provided by the Rand Global Circulation Model (GCM). Specifically, these variables include the surface pressure in addition to the temperatures and meridional and zonal winds at the levels of the GCM. The parameterization of the wave drag

in terms of the variables from the two-level model required assumptions to be made about the atmospheric wind and temperature profiles. Once these assumptions were made, the atmospheric response function and the wave drag could be characterized by studying the response of many atmospheres taken from a previous run of the Global Circulation Model.

The program during the past six months involved a series of tasks all leading to the parameterization of the lee wave drag. A subroutine will be delivered to the Rand Corporation by the end of the contract period to be tested and subsequently incorporated into the GCM. The below tasks were completed during this contract period:

1. We became familiar with the ARPA network and made our codes compatible with the system.

2. A prescription for the atmospheric wind and temperature profiles was selected.

3. The atmospheric response function code was rewritten and optimized.

4. The code for calculating the stress was written.

5. The topography spectrum function was run and studied for varied topographies.

6. The atmospheric response function was characterized in terms of data from the two-level model.

7. The stress integral was studied as a function of topography.

8. The component of the stress in the direction of the meridional winds was characterized, and a subroutine based on an analytic model has been formulated.

The same problems which plagued the mesoscale program also effected the work on the radiation codes. Most of the work performed during this period involved making the codes compatible

with the IBM 360/91 system and performing trial calculations to check out these codes. Modifications to the codes were made in preparation for the delivery of these codes to the Rand Climate Dynamics Group.

## 1. CHOICE OF WIND AND TEMPERATURE PROFILES IN THE ATMOSPHERE

The amplitude of the waves generated on the leeward side of mountains and the mechanism for the dissipation of these waves will depend strongly on the atmospheric wind and temperature profiles. In the linearized theory, the propagation of wave energy in the wave with horizontal wavenumbers $(k,l)$ is dependent on the Scorer parameter profile in the atmosphere. The Scorer parameter $l^2(z) = N^2/U_n^2 - d^2U_n/dz^2$ is a function of the atmospheric stability, $N$, and the velocity component, $U_n$, parallel to the wavevector. The amplitude of the waves that the atmosphere can support is determined by a solution of the equation

$$(d^2w/dz^2) + (l^2(z) - \kappa^2) w = 0 \qquad (1.1)$$

subject to the boundary conditions imposed by the model used. [1-5] In equation (1.1), $\kappa^2 = k^2 + l^2$. The local magnitude of the Scorer parameter, $l^2(z)$, with respect to the square of the magnitude of the wavevector, $\kappa^2$, will determine the amplification of a particular wavenumber. When the wind speed in the direction of the wavevector is very high, horizontal energy and momentum is pumped into that wavenumber, and the wave will grow in amplitude in that layer. Conditions producing amplification of wave energy $(\kappa^2 > l^2(z))$ also occur when the lapse rate approaches the adiabatic lapse rate. The longer waves will not be as greatly influenced by changes in the resonance characteristics of the lower atmosphere, and much of this wave energy will pass through the troposphere forcing the natural modes of the stratosphere.

The generation and dissipation of lee waves in an atmosphere will depend upon the fine structure of the wind field and the temperature profile. The response characteristics of the atmosphere to a disturbance with wavenumber $(k,l)$ is determined by the local stability of the atmosphere, the wavelength of the disturbance, and the angle the wavevector makes with the meridional and zonal winds. The most favorable conditions for the generation of high amplitude waves occur with strong low-level winds and a low-level inversion. The dissipation of the waves will occur at regions of low Richardson's number, that is, regions of high stress. The effect of horizontal stress on the wave is to turn the wavevector in the horizontal direction.[6] As the intrinsic frequency of the wave, $\omega - U_n \kappa$, goes to zero, the amplitude decreases and the momentum is given to the flowfield. Hence, an accurate description of the momentum transport to the atmosphere requires a detailed atmospheric temperature and wind velocity profile.

The modeling of the wavedrag associated with mountains is restricted by the lack of vertical and horizontal resolution of a global circulation model. We can resolve the topography to the 5' or 30' grid data available, but we rely on the atmospheric variables from the GCM for a definition of the atmospheric profiles of temperature and wind velocity. The wind vectors and temperatures are resolved to only the 4° by 5° grids used in the GCM. The strong low-level inversions (which, in any case, could not be resolved in the vertical by a two-level model) are generally the result of the movement of a warm air mass over a cold air mass. The resolution of frontal activity cannot be obtained explicitly from the GCM. However, arguments for the occurrence of inversions and a parameterization of the inversion level may be possible from a study of the movement of synoptic scale air masses in the GCM. We have not had the opportunity to attempt such a parameterization in this contract period, but an approach

of this type could improve the horizontal and vertical resolution of the atmospheric conditions. Our lee-wave model is limited by the resolution of the topography data available and not by the 4° by 5° grids of the GCM. Any arguments which would improve the resolution of the wind and temperature data would improve the treatment of the wave drag.

The wave drag model that we are applying is the linear, steady-state, adiabatic, Boussinesq formulation of Bretherton.[1] The momentum flux, in this model, is independent of height in the atmosphere except at critical layers where dissipation of the momentum occurs. The boundary conditions of the model do not permit reflection of waves and complete absorption of a wave will occur at a critical layer. The response of the atmosphere is determined by a solution of equation (1.1) subject to the boundary conditions,

$$
\left.
\begin{aligned}
\frac{dw}{dz} &= -\sqrt{k^2 - 1^2(H)}\, w \\
\text{or} \quad \frac{dw}{dz} &= i\sqrt{1^2(H) - k^2}\ \mathrm{sgn}(U_n)w,
\end{aligned}
\right\}
\tag{1.2}
$$

applied at the level $z = H$ where the calculation is begun. The first condition in equation (1.2) is applied when the wavenumber $\kappa^2$ is greater than the Scorer parameter at $z = H$ and represents exponential decay of the wave amplitude above the cutoff height. The second condition is applied when the Scorer parameter is greater than the wavenumber and represents a radiation condition in which the waves continue to propagate upward through the layer at $z = H$. A detailed discussion of this model has been given in previous reports.[7,8]

The effort during this phase of the contract period has been directed at characterizing the stress integral and determining to what degree the integrands of the two components of the stress could be simplified. In characterizing the stress

5

integral, we have chosen to fit the GCM wind speed and temperature data at the two levels with prescribed vertical profiles which will be described subsequently. The Scorer parameter profile for each wavevector then followed from the definition of the Scorer parameter and the atmospheric response was determined by integration of equation (1.1) through the atmosphere subject to the boundary conditions at the top of the atmosphere given in equation (1.2). The wind profiles, the temperature profiles, and the Scorer parameter, are of necessity considerably smoothed due to the poor resolution of the GCM. Since the Scorer parameter is considerably smoothed, we might have alternately chosen to express the Scorer parameter in terms of the mathematical forms which give analytic solutions to the Scorer equation. Application of these analytic solutions to multilayer models for the one-dimensional problem has been given by Palm and Foldvik and Vergeiner.[9,10] The same solutions are applicable to our problem if the Scorer parameter is treated as a function of the wavevector of each of the components of the topography spectrum function. The Scorer equation admits analytic solutions when the Scorer parameter is treated as a constant through the layer, as an exponential function of height, or if it is taken to be

$$l^2(z) \equiv l_0^2 - \frac{2}{(z+\alpha)^2} \tag{1.3}$$

where $l_0$ and $\alpha$ are constants determined for each level. The form given in equation (1.3) has been applied by Vergeiner. We will discuss in Section 3 how we intend to use the analytic solutions in the Rand GCM subroutine to calculate the two components of the wave drag. We did not feel justified in using these analytic models during this phase of the contract period because of the need to study the sensitivity of the atmospheric response function to the changes in the atmospheric variables.

6

SSS-R-74-2331

## 1.1  The Choice of the Wind Profile

We have described the difficulties involved in obtaining
the meridional and zonal wind profiles.  We inspected the wind
data that were available on National Weather Service tapes,[11]
obtained data available on microfilm from the National Center
for Atmospheric Research, and reviewed the seasonally averaged
wind profiles available from the National Weather Records Center.[12]
We also consulted with meteorologists to obtain suggestions on
how the wind profiles might be deduced from the two-level model.

In Figures 1 and 2 we have reproduced typical seasonally
averaged data from the National Weather Records Center data for
the midlatitudes over mountainous terrain.   Each component is
characterized by peak speeds near the tropopause and can be ap-
proximated by a second-degree polynomial.

Wind speed and direction data obtained from the National
Center for Atmospheric Research are reproduced in Figure 3.
These data represent soundings over the Rocky Mountains taken
over a period of approximately one hour.

Finally, in Figures 4 to 6 we have reproduced data taken
from the National Weather Service tapes for the meridional and
zonal winds and the temperature profiles over West Virginia.
The data are represented by the dots and the data points have
been fitted with a smooth curve.

In this parameterization study the solution of the Scorer
equation was obtained by an integration of the equation through
the atmosphere in the z-coordinate system.  To use the GCM data
required a transformation from the $\sigma$-coordinate system to the
z-coordinate system and extrapolation of the data to other points
in the atmosphere.  The temperature, given at the $\sigma = 1/4$ and
$\sigma = 3/4$ levels, was extrapolated in a pressure coordinate system
by letting

7
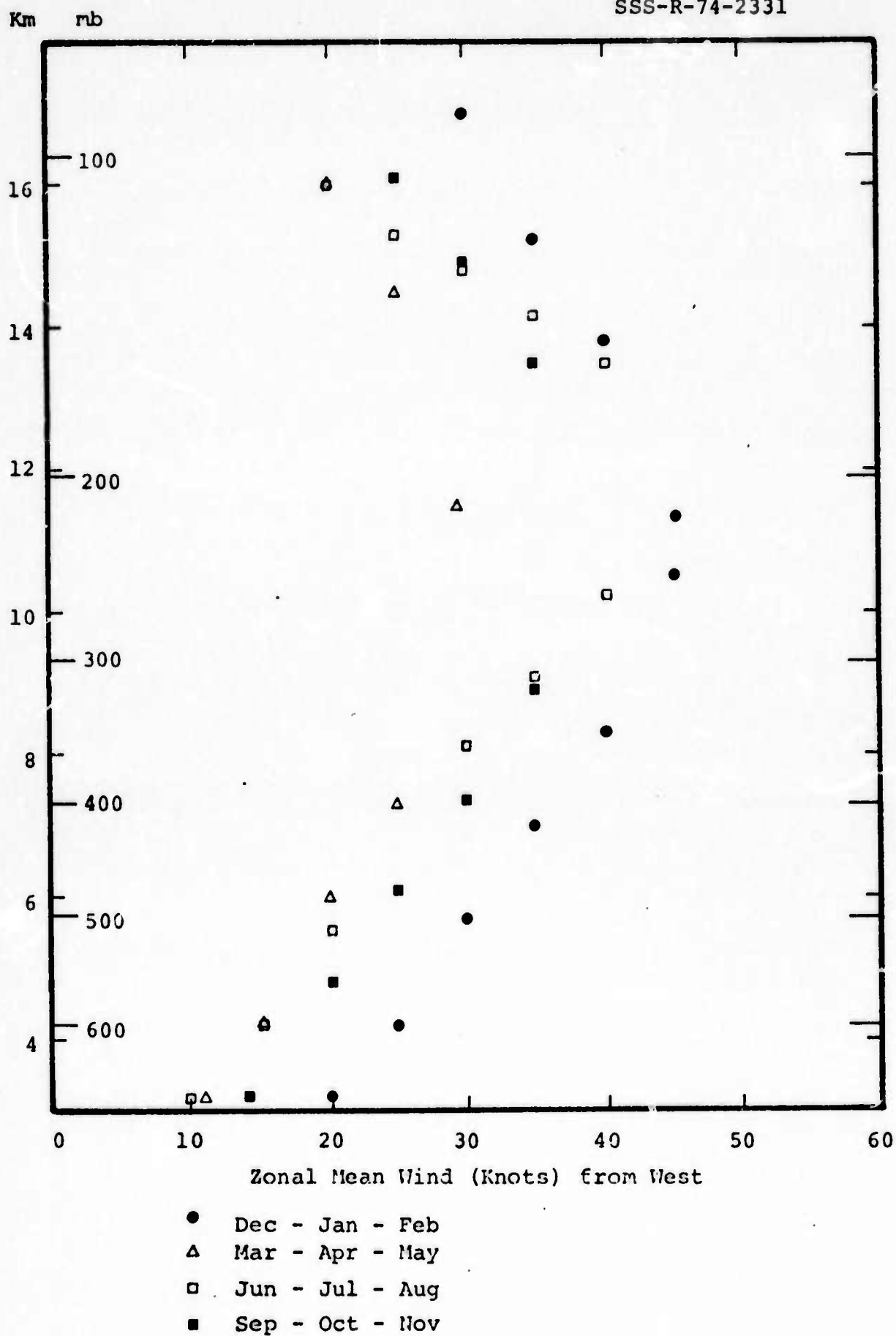
Figure 1.    Seasonally averaged zonal mean wind at 110°W 45°N
             from U.S. Department of Commerce Technical Paper 41.

8
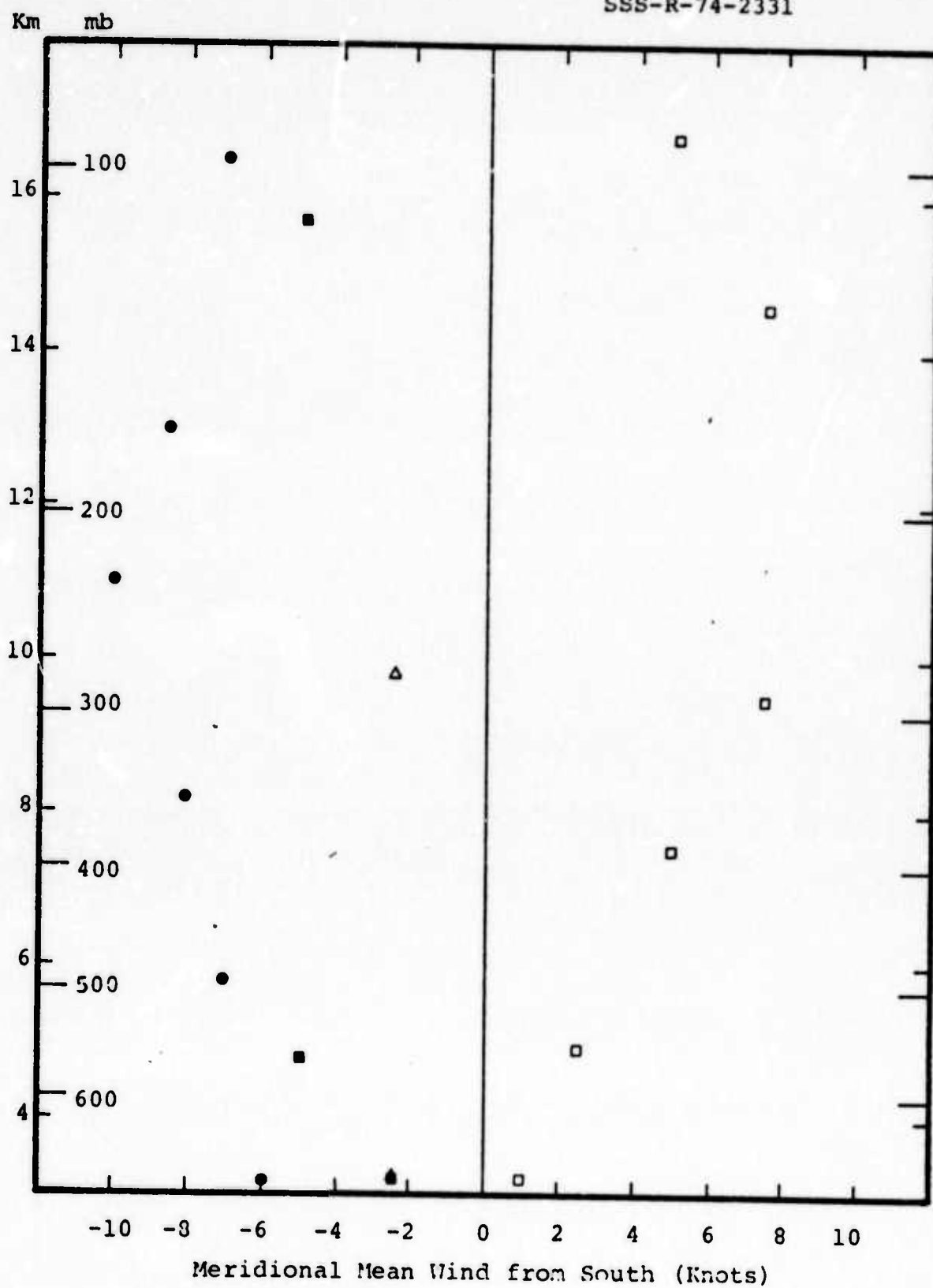
Figure 2.   Seasonally averaged meridional mean wind for 110°W
45°N from U.S. Dept. of Commerce Technical Paper 41.
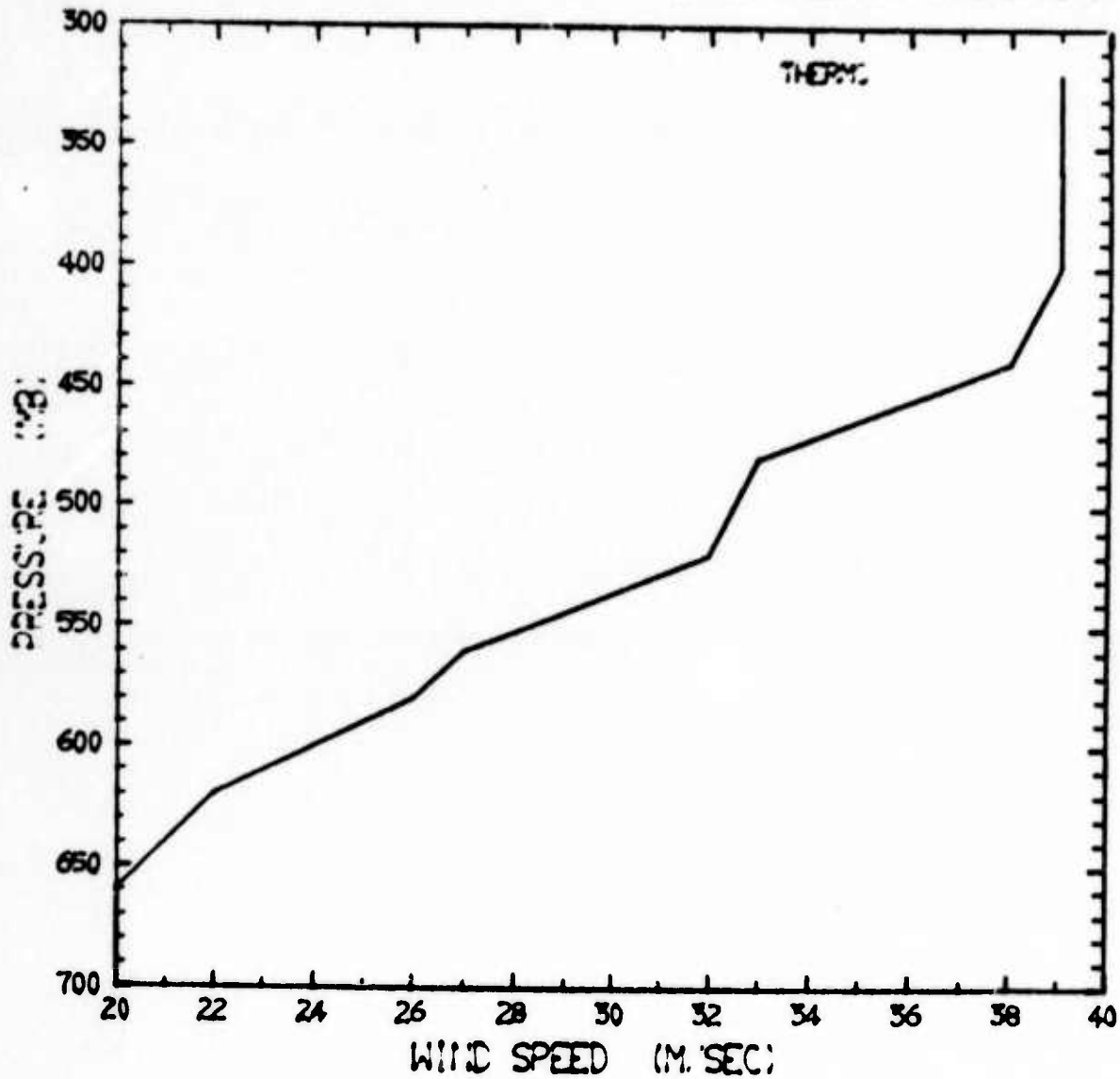
Figure 3a.   Wind speed data from NCAR for March 12, 1973.
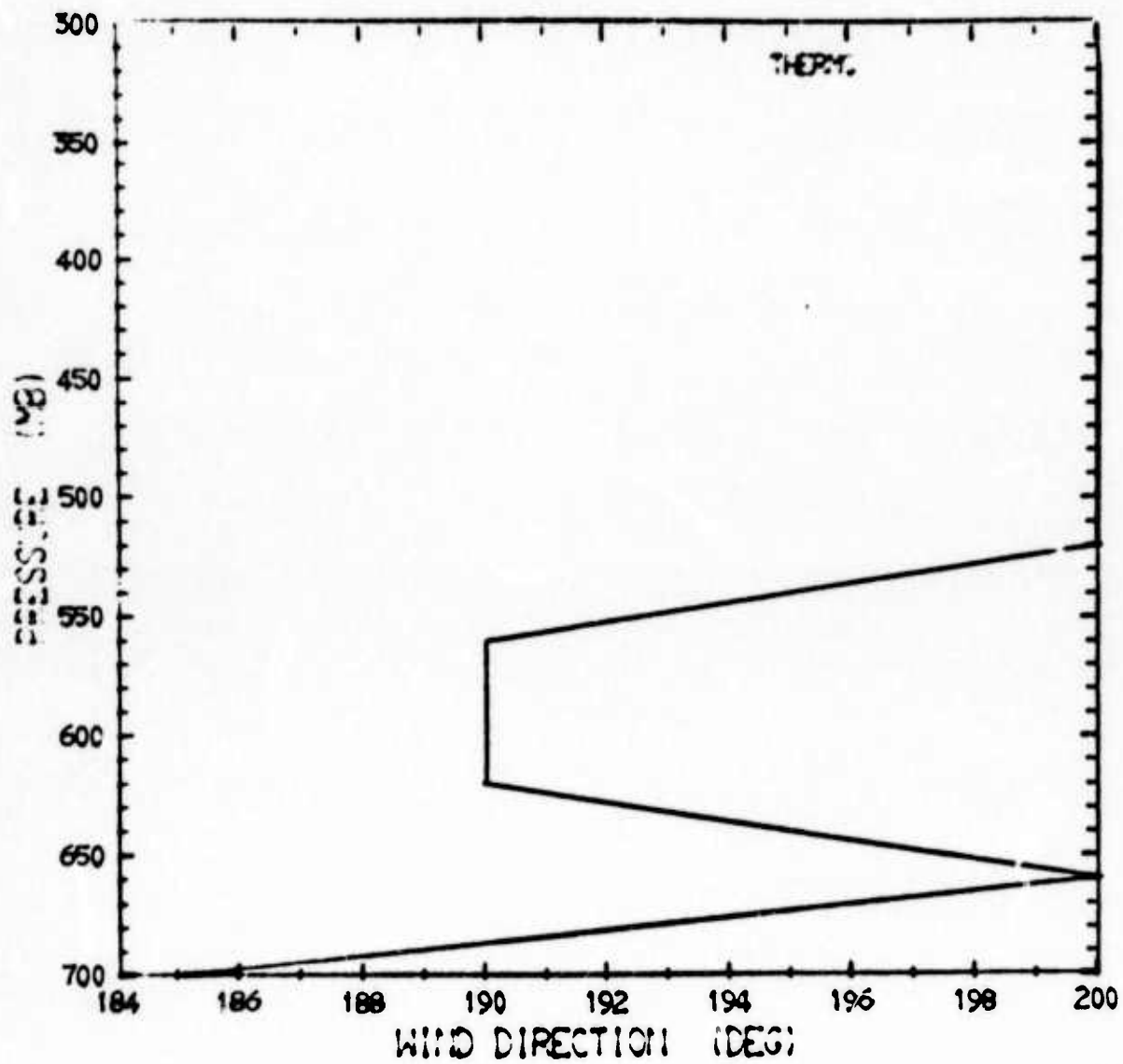
Figure 3b.  Wind direction data from NCAR for March 12, 1973.
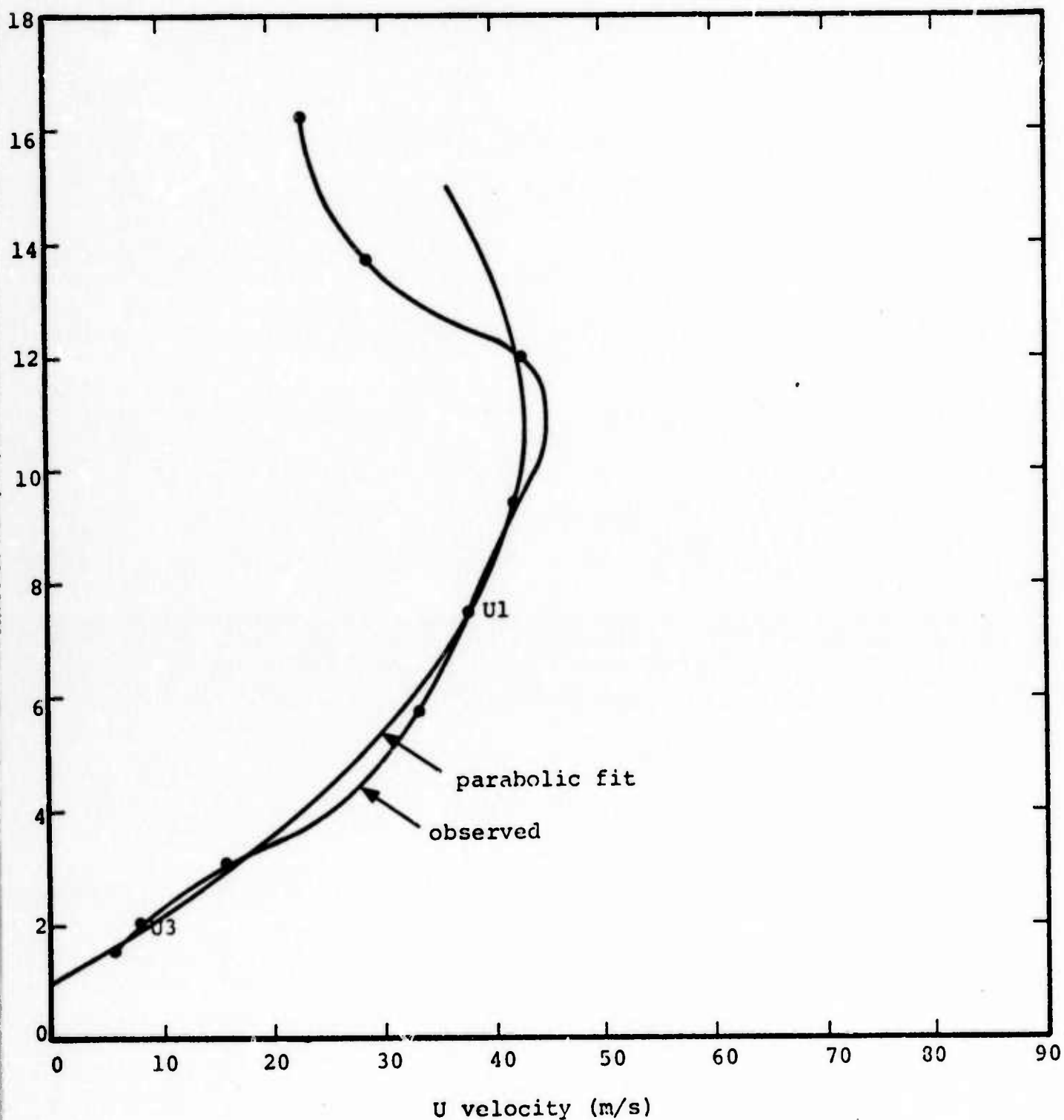
Figure 4. The zonal wind profile for West Virginia from the National Weather Service tapes.
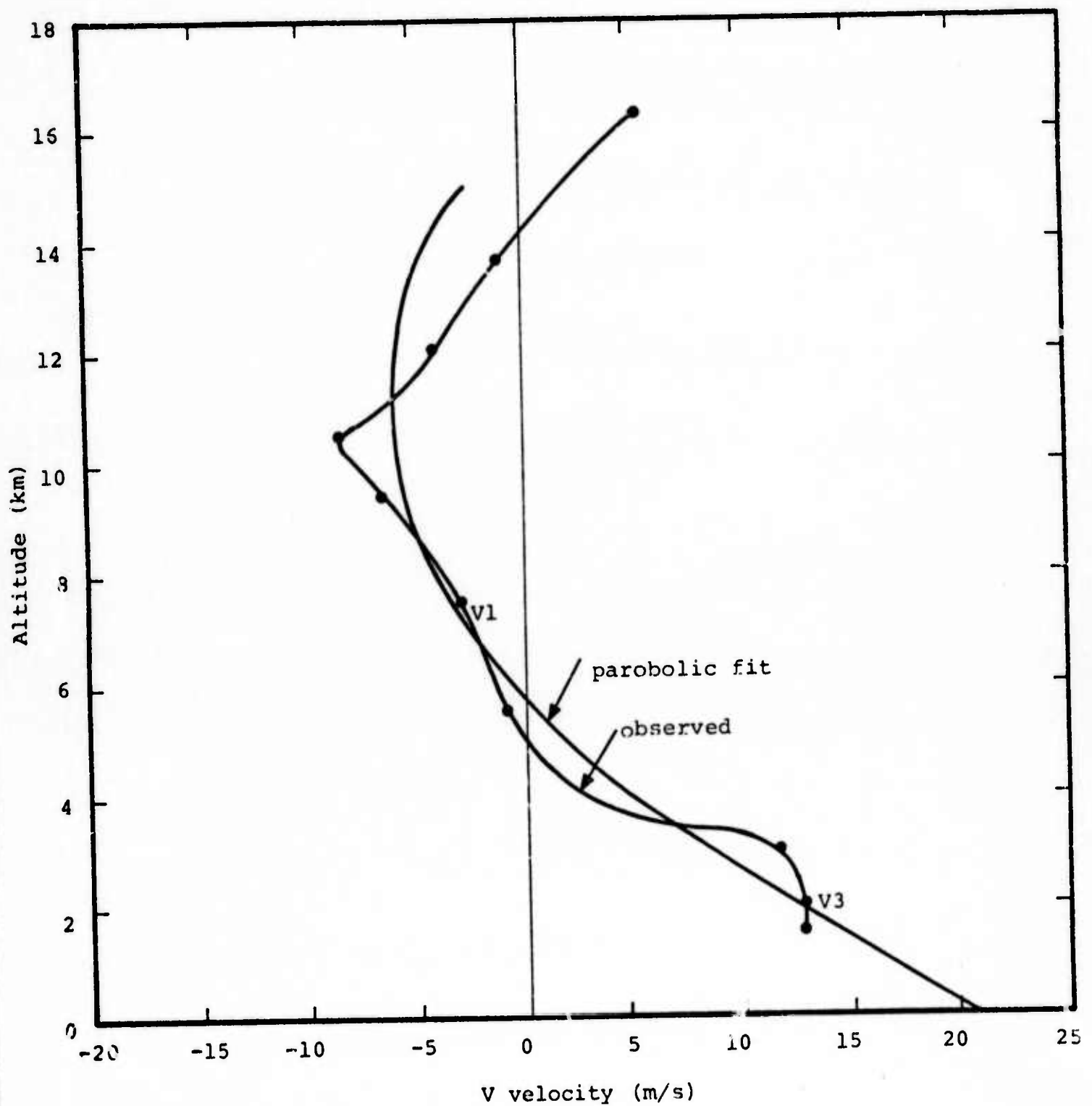
Figure 5.   The meridional wind profile for West Virginia from the National Weather Service tapes.
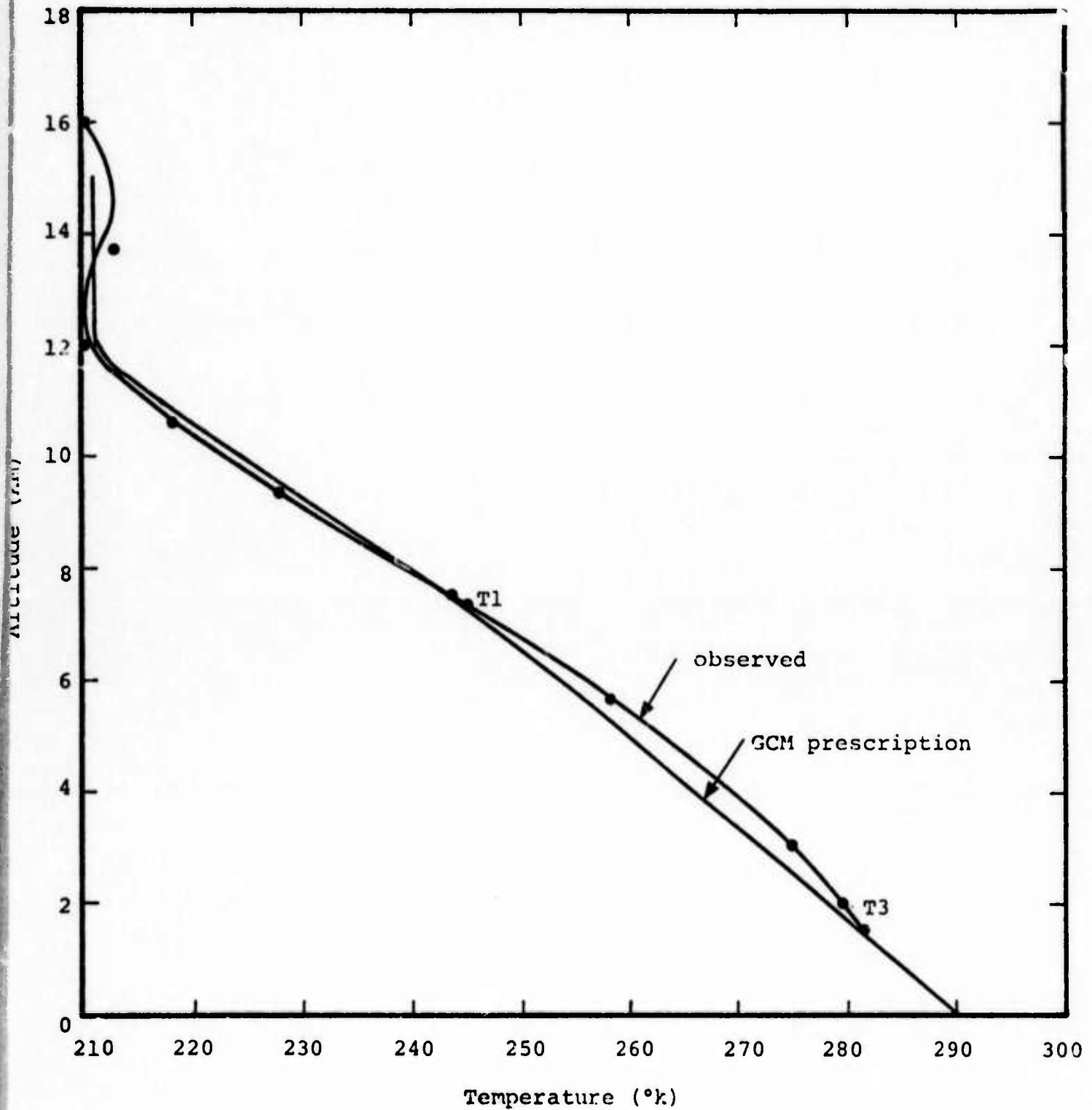
Figure 6. The temperature profile for the West Virginia data
taken from the National Weather Service tapes.

SSS-R-74-2331

$$T(p) = \frac{p^{k_1}}{p_3^{k_1}-p_1^{k_1}}\left\{\frac{T_1}{p_1^{k_1}}\left[p_3^{k_1}-p^{k_1}\right] + \frac{T_3}{p_3^{k_1}}\left[p^{k_1}-p_1^{k_1}\right]\right\} \qquad (1.4)$$

below the 200-mb level and assuming an isothermal layer above this level. In equation (1.4), $k_1 = 0.286$, and subscripts 1 and 3 denote the variables at the $\sigma = 1/4$ and $\sigma = 3/4$ levels, respectively. The transformation from the p-coordinates to the z-coordinates followed by successive application of the hydrostatic equation written in finite difference form. The pressure profile obtained in this manner from the West Virginia data is given in Figure 7.

The profiles of the meridional and zonal winds were obtained by a parabolic fit, in z-coordinates, of the wind data points at $\sigma = 1/4$, $\sigma = 3/4$, and a third point obtained by a reflection of the $\sigma = 1/4$ data point about the 200-mb pressure level. This profile closely approximates the profiles of the seasonally averaged meridional and zonal winds in the midlatitudes. In Figures 4 to 6 we have applied the extrapolation schemes to the West Virginia wind and temperature profiles. In this particular example, very high surface winds are predicted by this model. We did not correct for the high surface winds because in general this was not a problem. The only advantage of this prescription for the winds is that it provides an extrapolation above 200 mb which is not given by the linear extrapolation in the GCM. A prescription for the wind field which more accurately treats the variability of the winds with height would require a lengthy statistical treatment of the available wind data in terms of the two levels of the GCM. The additional information gained by such a prescription would undoubtedly be lost in the parameterization required to reduce the computing time to levels compatible with the GCM. A simple modeling of the wind field is consistent with the requirements of a simple mathematical expression for the Scorer parameter to

15
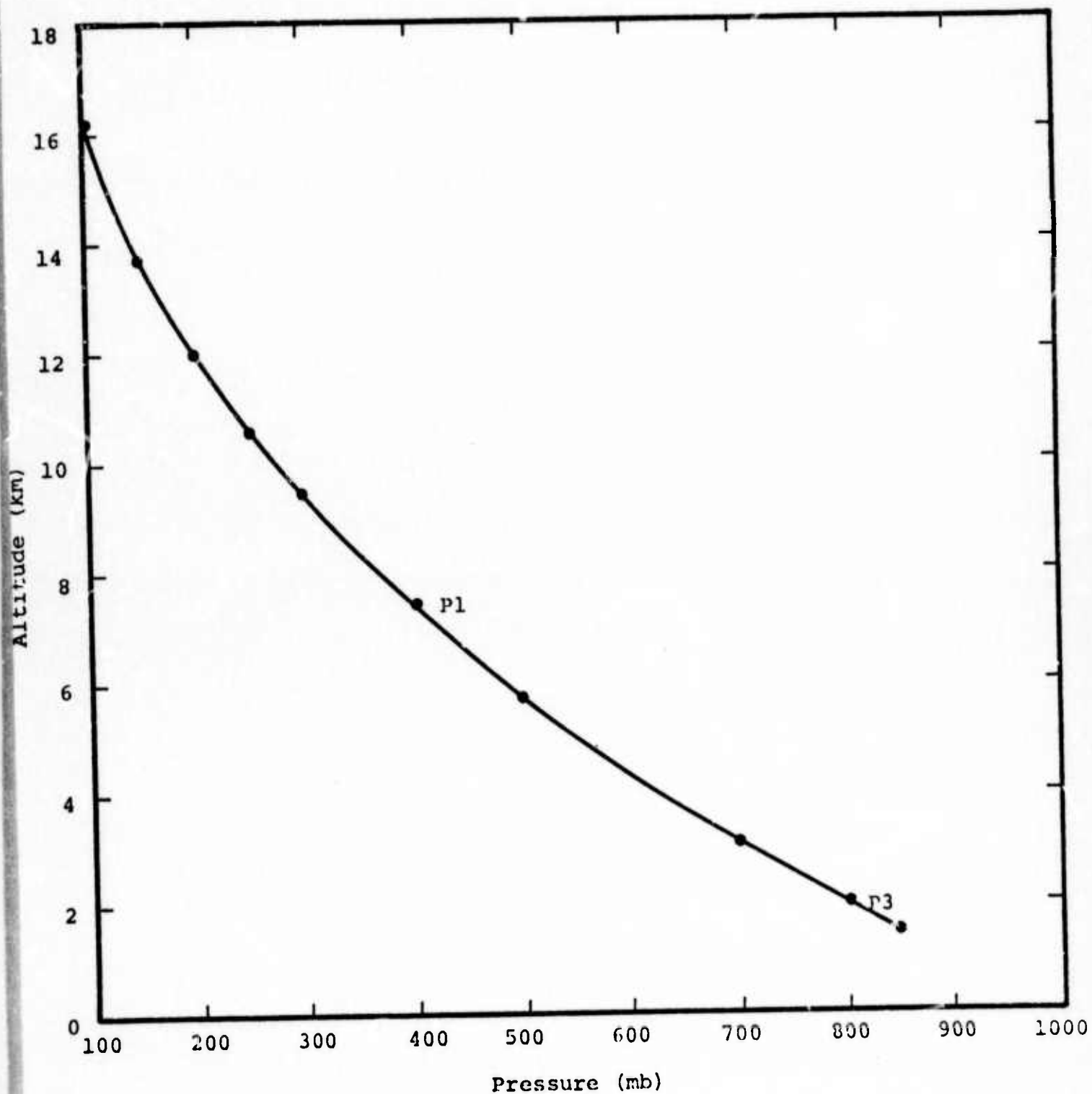
Figure 7. The pressure profile for West Virginia from the National Weather Service tapes.

obtain an analytic solution of the Scorer equation. In general, in the absence of very stable conditions, the Scorer parameter will be much larger than the wavenumbers resolvable in the topography spectrum. Any local decrease of the Scorer parameter will have a greater influence on the shorter wavelengths than on the long wavelengths. Other investigators have found that these trapped waves do not increase the wave drag significantly.[1,13]

## 1.2 Choice of the Temperature Profile and Its Effect on the Atmospheric Response

The temperatures at the $\sigma = 1/4$ and $\sigma = 3/4$ levels have been extrapolated to other levels by assuming that the potential temperature is linear in $p^{k_1}$, where $k_1 = 1 - 1/\gamma$ and $\gamma$ is the ratio of specific heats for the atmosphere. We have extended this to the 200-mb level, and then we have assumed an isothermal atmosphere above this level. The extrapolation of the temperature is the same as used in the GCM.

The temperature profile enters explicitly in the Scorer equation through the stability. It also enters into the wind profile through the transformation of the $\sigma$-coordinate system to the z-coordinate system by the hydrostatic equation. The smoothing of the temperature profile should also have a more significant effect on the shorter wavelengths than on the long wavelengths.

## 2. BEHAVIOR OF THE STRESS INTEGRALS

We have described the linear, steady-state Bretherton model in detail in previous reports[7,8] and have derived the stress integrals in terms of the atmospheric response function and the topography spectrum function. In this section we describe the results of parameterization studies intended to lead to a subroutine for the mountain lee wave drag compatible with the Rand Global Circulation Model. We have considered the ten

topographic grids and the 15 atmospheres listed in Tables 1 and 2. All of the grids listed in Table 1 were 2°40' on a side. In addition, another computer run was made of the stress integral on a 4° by 5° grid with the northwest corner located at 121° W 37° N. The smaller grids were selected for the economy of calculating fewer values of the atmospheric response function. The atmospheres were taken from selected mountainous areas of a GCM run. Four atmospheres were taken from this GCM run and the remaining 11 atmospheres are perturbations or permutations of these four sets of data.

The topography spectrum function, the atmospheric response function, and the stress integral are discussed in the next three sections. Our objective was to parameterize the stress integral; therefore, much of the discussion in the third section is devoted to the investigation of individual components of the stress integral and their dependence on the atmospheric response function and the topography spectrum function.

## 2.1 The Topography Spectrum Function

Very little time was spent trying to characterize the topography spectrum function in terms of the features of the terrain. We decided early in the parameterization that the spectrum function could be calculated and stored for the grids on which the wave drag was to be calculated. The two-dimensional spectrum of the real topography is not easily related to features of the terrain.

The topography spectrum function is, by definition,

$$A(k,l) = \frac{4\pi^2}{XY} \hat{h}^*(k,l) \, \hat{h}(k,l)$$

where X and Y are the dimensions of the grid and h(k,l) is the two-dimensional Fourier transform of the topography,

TABLE 1
ATMOSPHERES STUDIED

| ATMOSPHERE | $P_s$ | $T_1$ | $T_3$ | $U_1$ | $U_3$ | $V_1$ | $V_3$ |
|---|---|---|---|---|---|---|---|
| 1 | 906.4 | 231 | 263 | 29.3 | 7.88 | -0.97 | 0.82 |
| 2 | 826.0 | 234 | 262 | 33.6 | 14.80 | 4.57 | -0.69 |
| 3 | 906.4 | 231 | 263 | 29.3 | 7.96 | -0.97 | 0.82 |
| 4 | 906.4 | 231 | 263 | 29.3 | 8.27 | -0.97 | 0.82 |
| 5 | 826.0 | 234 | 262 | 33.6 | 15.00 | 4.57 | -0.69 |
| 6 | 826.0 | 234 | 262 | 33.6 | 14.60 | 4.57 | -0.69 |
| 7 | 826.0 | 234 | 262 | 33.6 | 15.50 | 4.57 | -0.69 |
| 8 | 826.0 | 234 | 262 | 33.6 | 14.10 | 4.57 | -0.69 |
| 9 | 826.0 | 234 | 262 | 33.6 | 16.30 | 4.57 | -0.69 |
| 10 | 826.0 | 234 | 262 | 33.6 | 13.30 | 4.57 | -0.69 |
| 11 | 906.4 | 231 | 263 | 33.6 | 14.80 | -0.97 | 0.82 |
| 12 | 906.4 | 231 | 263 | 29.3 | 7.88 | 4.57 | -0.69 |
| 13 | 743.8 | 214 | 237 | -4.95 | -2.89 | 11.47 | 5.85 |
| 14 | 738.9 | 239 | 267 | 10.95 | 5.14 | 13.23 | -4.93 |
| 15 | 743.9 | 239 | 267 | -4.95 | -2.89 | 11.47 | 5.85 |

## TABLE 2
## TOPOGRAPHIES INVESTIGATED

| TOPOGRAPHY | NORTHERN LATITUDE | SOUTHERN LATITUDE | WESTERN LONGTIUDE | EASTERN LONGITUDE |
|:---:|:---:|:---:|:---:|:---:|
| 1 | 37°N | 34° 20'N | 121°W | 118° 20'W |
| 2 | 37°N | 34° 20'N | 118° 20'W | 115° 40'W |
| 3 | 37°N | 34° 20'N | 115° 40'W | 113°W |
| 4 | 37°N | 34° 20'N | 113°W | 110° 20'W |
| 5 | 37°N | 34° 20'N | 110° 20'W | 107° 40'W |
| 6 | 37°N | 34° 20'N | 107° 40'W | 105°W |
| 7 | 37°N | 34° 20'N | 105°W | 102° 20'W |
| 8 | 37°N | 34° 20'N | 102° 20'W | 99° 40'W |
| 9 | 37°N | 34° 20'N | 99° 40'W | 97°W |
| 10 | 37°N | 34° 20'N | 97°W | 94° 20'W |

$$\hat{h}(k,l) = \frac{1}{4\pi^2} \int_0^X \int_0^Y h(x,y)\, e^{i(kx+ly)}\, dxdy\ .$$

The function $A(k,l)$ depends strongly on the amplitude of a
Fourier component of the topography and will therefore vary
over many orders of magnitude. The 5' topography data which we
have over North America provides resolution of the topography
spectrum to a wavenumber of $0.3\ km^{-1}$ in the midlatitudes. We
will consider the wavenumber dependence of the topography in
detail in our discussion of the stress integral where the

20

amplitude of the spectrum function must be considered in the light of the dependence of the atmospheric response function on wavenumber.

## 2.2 The Atmospheric Response Function

In the Bretherton formulation of the wave drag the atmospheric response function represents the response of the atmosphere independent of the forcing conditions at the lower boundary. If the wave vectors are written in polar coordinates the response of the atmosphere in the continuous regime has been shown to be

$$F(\kappa,\phi) = \frac{\kappa}{2i}\left|\frac{dw}{dz} w^*(z) - \frac{dw}{dz} w(z)\right| \Bigg/ w^*(0) \, w(0) \qquad (2.1)$$

where $w(z)$ represents the amplitude of the wave motion. The solution for $w(z)$ is obtained by integrating Eq. (1.1) through the atmosphere subject to the boundary conditions given in Eq. (1.2). By multiplying the complex conjugate of Eq. (1.1) by $w$ and subtracting the product of $w^*$ and Eq. (1.1) it is easily shown that Eq. (2.1) is independent of the $z$. Equation (2.1) can then be simplified by evaluating the numerator at the upper boundary. The result,

$$F(\kappa,\phi) = \frac{2\sqrt{\ell^2(H) - \kappa^2}}{w_R^2(0) + w_I^2(0)} \, \text{sgn}[U_n(H)] \quad , \qquad (2.2)$$

has been programmed into our atmospheric response function code.

From a physical point of view the atmospheric response function represents a measure of the kinetic energy that must be transferred from the mean flow to the vertical at the ground

21

level to propagate one unit of kinetic energy to the level at which the integration of the Scorer equation begins. Resonances in the atmospheric response function will occur when the kinetic energy, transferred into the vertical at the ground level, required to propagate one unit of energy into the stratosphere approaches zero.

Equation (2.2) illustrates one of the weaknesses of the model. The atmospheric response is a function of the height at which the integration of the Scorer equation begins. The dependence on the depth of the atmosphere appears explicitly in the numerator of Eq. (2.2). Of greater significance is the dependence of the denominator on the initial height, $H$, chosen to begin the numerical integration of the Scorer equation. Typically, the stability is on the order of $2 \times 10^{-4}$ sec$^{-2}$ and in some layers of the atmosphere, particularly near the ground, the wind speed is on the order of 1 m/sec. The Scorer parameter is then $2 \times 10^{-4}$ m$^{-2}$ and large variations of $w(0)$ will then occur when changes in $z$ on the order of $(\pi/2)(1.4 \times 10^{-2}$ m) or approximately 100 m are made. Perhaps because of this and for obvious reasons of computer economy, Bretherton defines a critical layer at points in the atmosphere where the Scorer parameter, $1^2(z)$, is greater than $2.5 \times 10^{-5}$ m$^{-2}$. His integration then begins from this point and no larger values of the Scorer parameter occur in the integration.

To be consistent in our studies we always began the integration at 15 km above sea level. The depth of the atmosphere was then determined by the average height of the terrain.

In addition to those atmospheres listed in Table 2, we investigated other atmospheres earlier in the contract period to characterize the behavior of the atmospheric response function. These atmospheres were obtained by making a linear interpolation between the data points taken from National Weather

22

Service tapes. Results of one of these runs are shown in
Figures 8 to 13. The atmospheric response function was run for
50 values of the wave vector magnitude, $\kappa$, and for 19 angles
between -90° and 90° from the direction of the zonal wind. The
atmospheric response function is invariant under the transfor-
mation from $(k,l)$ to $(-k,-l)$. Critical layers for this atmos-
phere occurred for angles around 77°. For $70° \leq \phi \leq 90°$, the
Scorer parameter is much larger than the magnitude of the wave
vector and $F(k,l)$ is virtually independent of $\kappa$ .

When atmospheric layers exist where $l^2(z) < \kappa^2$ , energy
will be pumped into that mode which propagates to that layer
and in phase with the atmospheric response at that layer. The
resonances which occur in the continuous spectrum in Figures
10 to 13 are associated with wave vectors such that $l^2(z) <$
$\kappa^2$ for a segment of the atmosphere. These resonances will not
have any effect on the stress calculated with the topography
data that is available to us. With 5' resolution the maximum
resolvable wavenumber in the topography spectrum is 0.3 $km^{-1}$
in the midlatitudes. In the upper atmosphere, where winds of
sufficient strength may be present to make the Scorer parameter
comparable to $\kappa^2$, the stability is typically $4 \times 10^{-4}$ $sec^{-2}$.
The winds required to give a Scorer parameter comparable to our
maximum resolvable wavenumber are on the order of 65 m/sec.
Without better resolution in the atmospheric variables it is
unlikely that the lapse rates or the winds required to have a
resonance in the atmospheric response function will be found.

In the absence of these resonances the atmospheric re-
sponse is nearly independent of $\kappa$ for a constant $\phi$ . Over
the entire range of $(\kappa,\phi)$ the atmospheric response changes by
less than two orders of magnitude compared to the topography
spectrum which may vary over seven orders of magnitude or more.
These observations considerably simplify the treatment of the
stress integrals and make it possible to neglect many of the
terms in the integral of the stress.
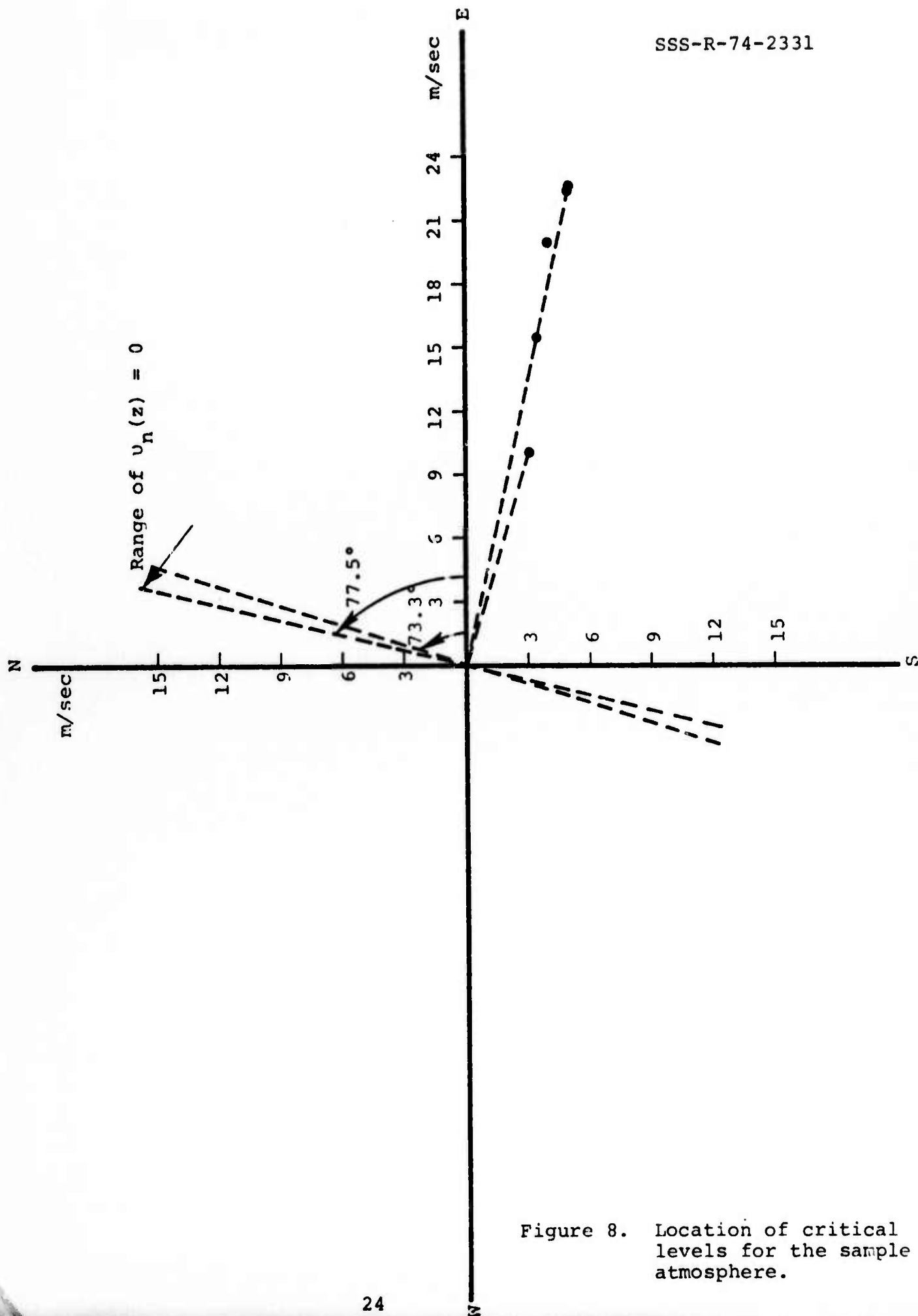
Figure 8.   Location of critical levels for the sample atmosphere.
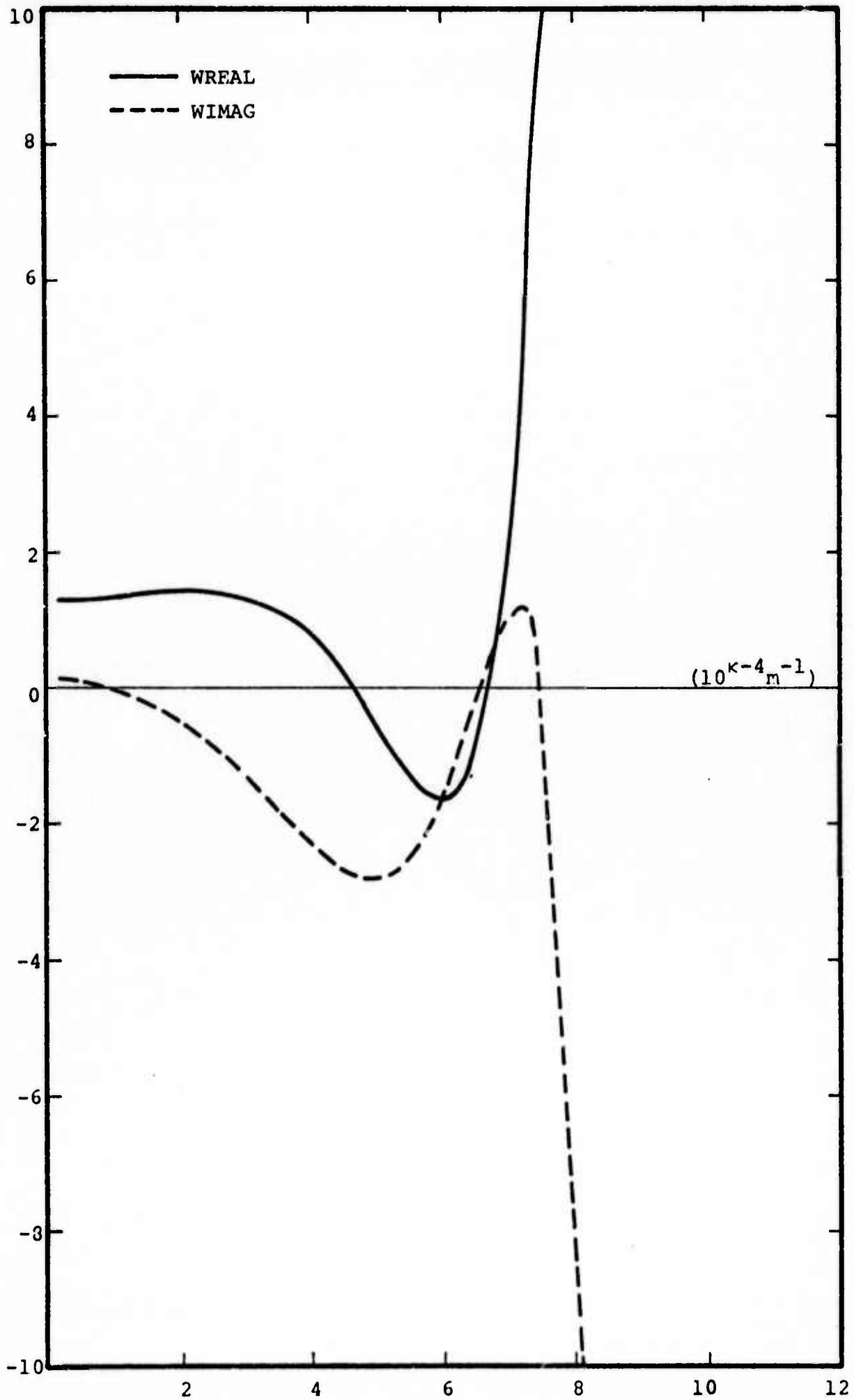
Figure 9.  The real and imaginary parts of the ground level wave amplitude for $\phi = 0$.
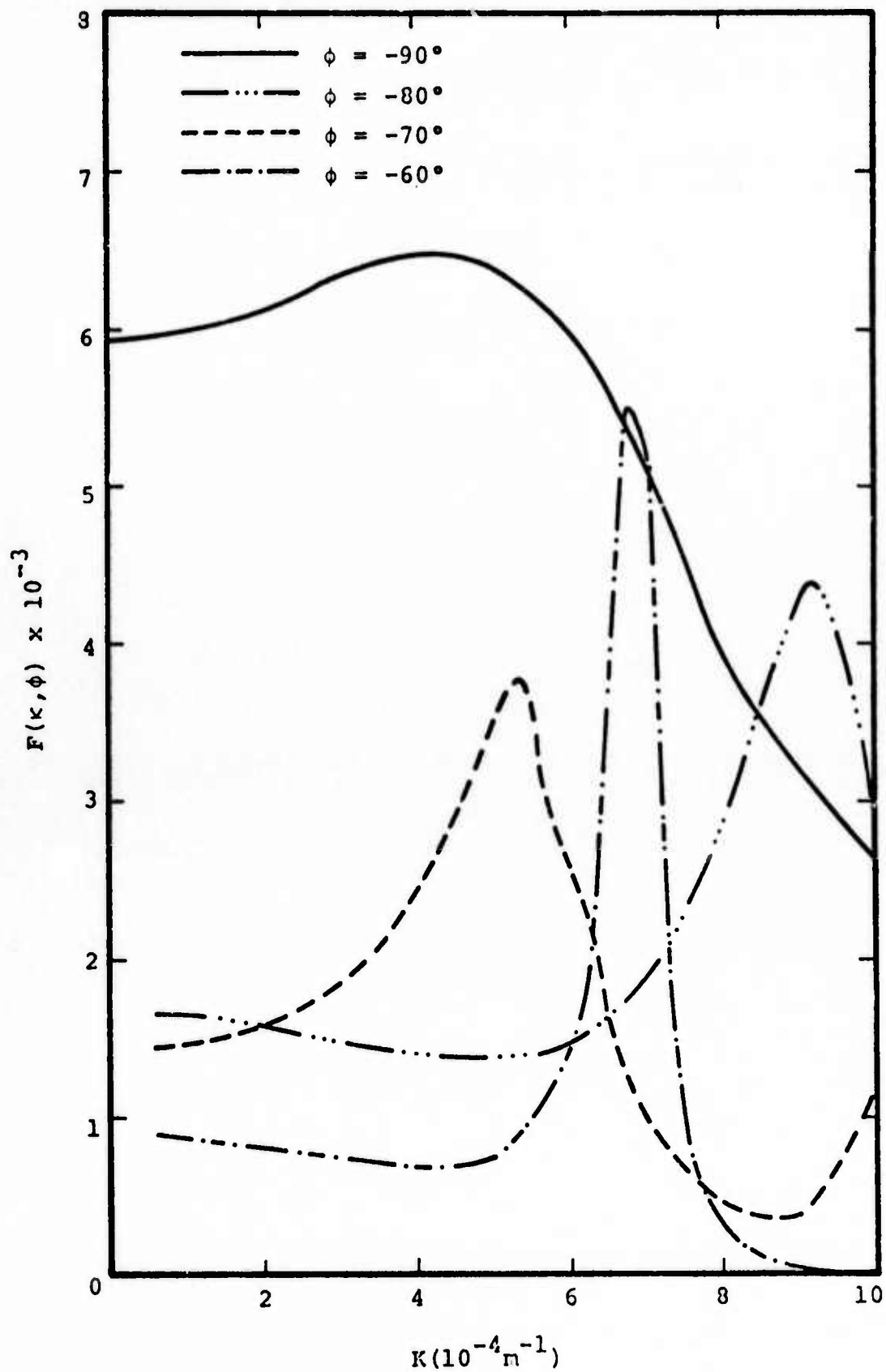
Figure 10. Wavenumber dependence of the atmospheric response
function for fixed angles of the wavevector.
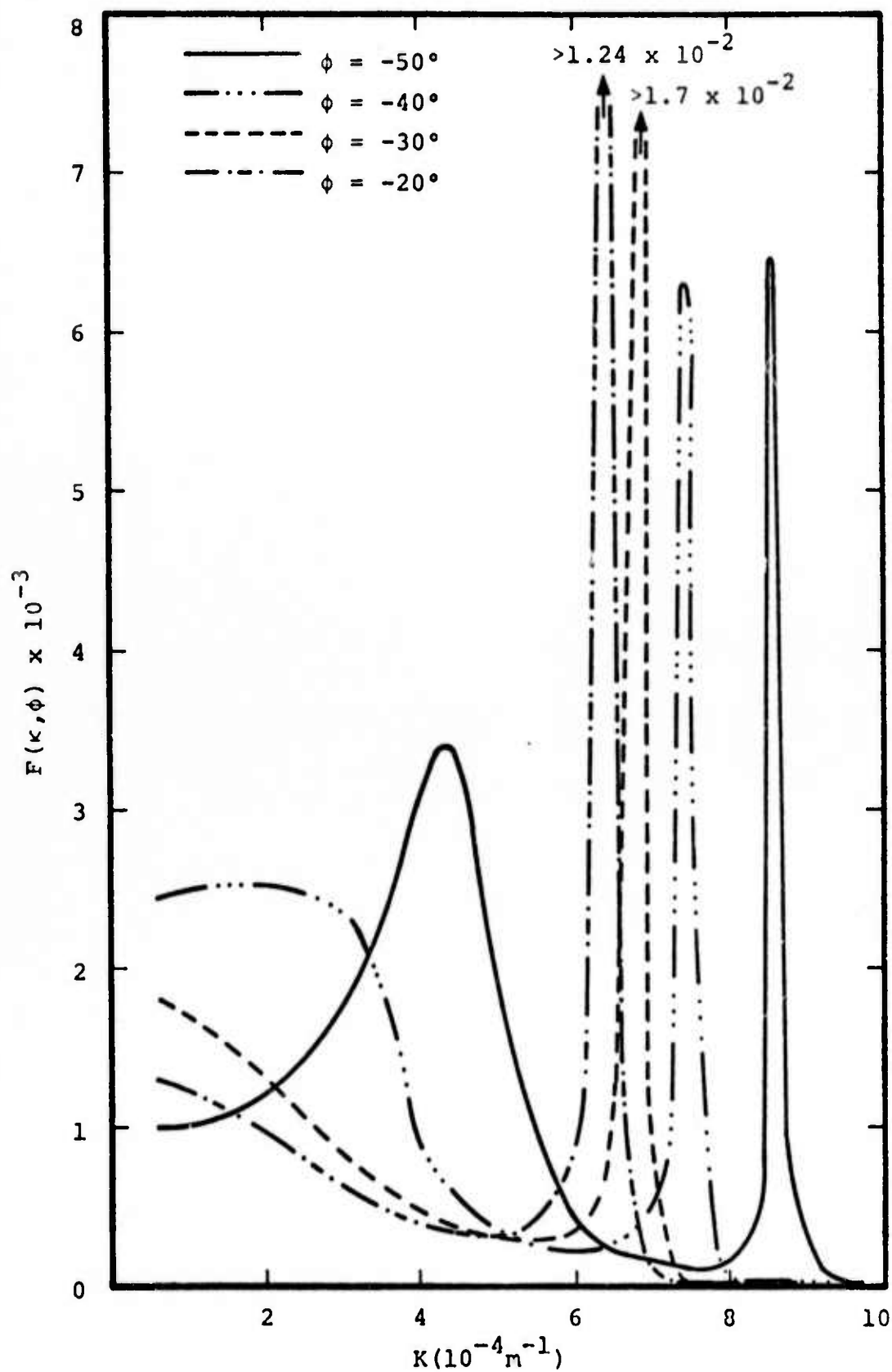
Figure 11. Wavenumber dependence of the atmospheric response function for fixed angles of the wavevector.
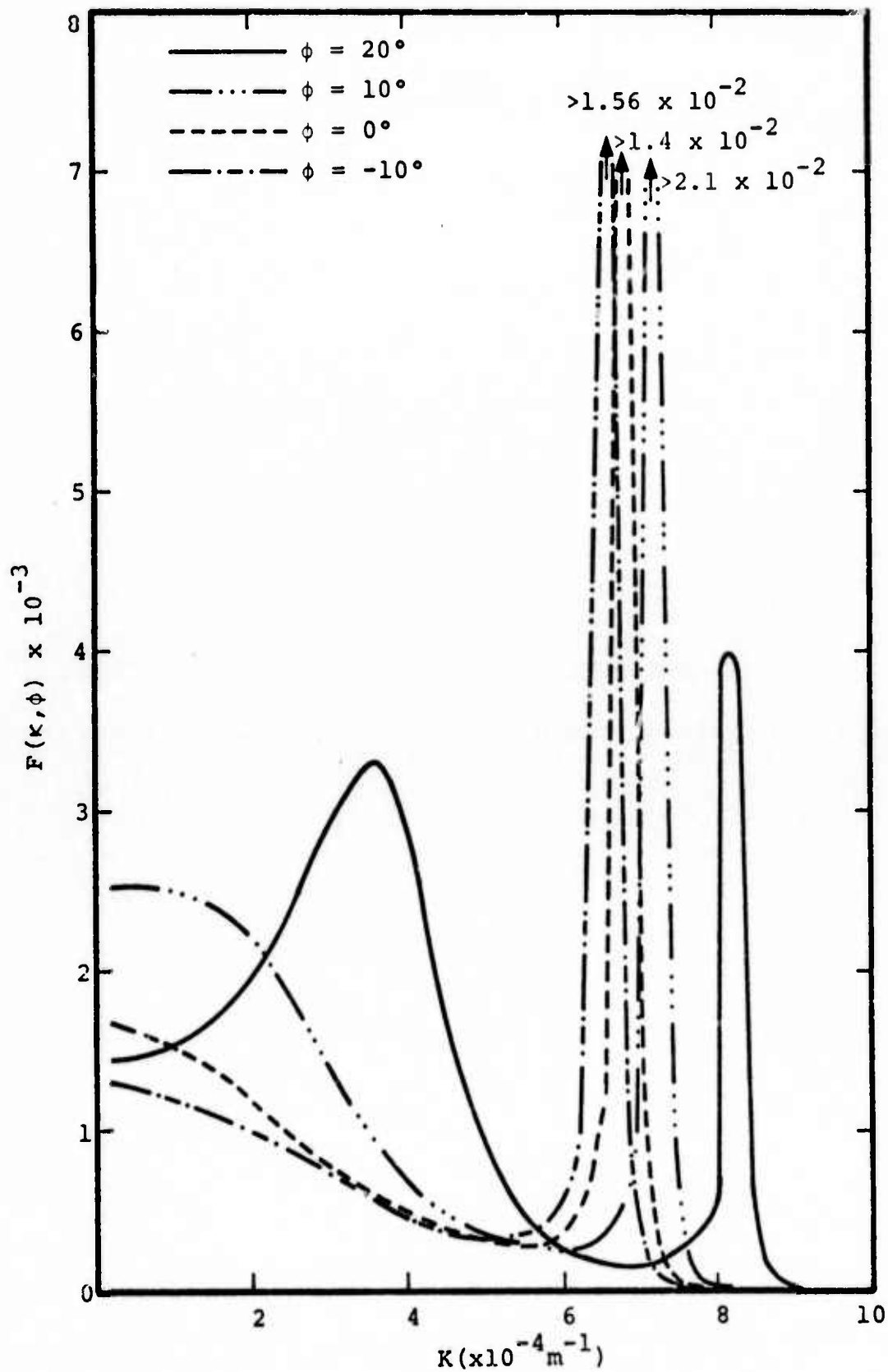
Figure 12. Wavenumber dependence of the atmospheric response function for fixed angles of the wavevector.
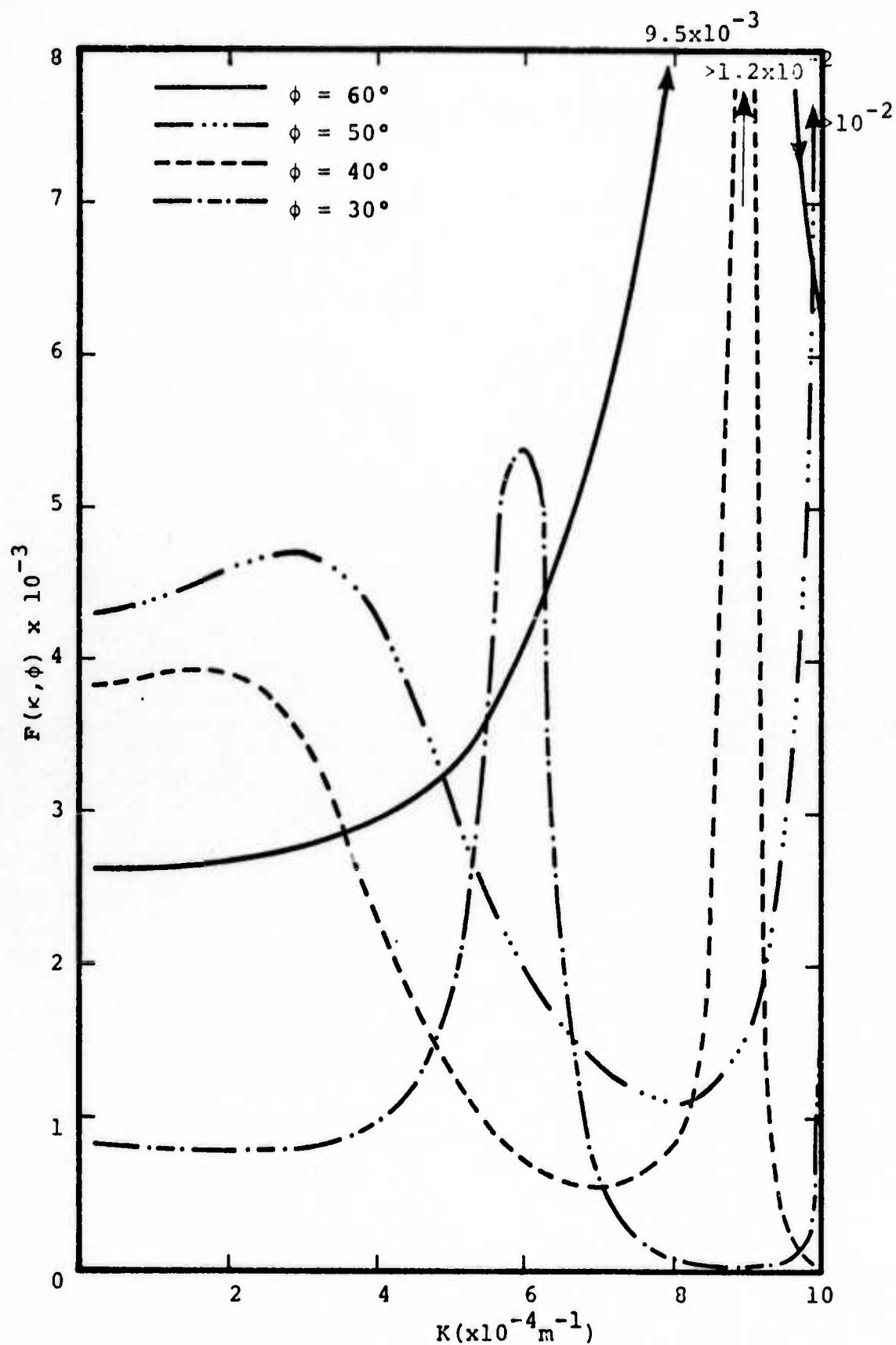
Figure 13.  Wavenumber dependence of the atmospheric response
function for fixed angles of the wavevector.

Before the beginning of the parameterization of the wave drag it was necessary to reduce the computing time required for the atmospheric response function. At the start of this contract period the computing time required to calculate the atmospheric response function for the 500 wavenumbers, required to integrate the stress integral, was 1100 seconds. By a judicious optimization of the code and a simplification of the numerical methods involved in the solution of the Scorer equation we reduced the time required to calculate the 500 values of $F(\kappa,\phi)$ to 20 seconds for our parameterization study. This optimization produced less than a 3% change in the magnitude of the calculated atmospheric response function.

## 2.3   The Calculation of the Stress Integral

During this contract period the codes for calculating the two components of the sress were developed. The code was written to perform the integration in horizontal wave number space; the range and resolution of the wave numbers being determined by the resolution of the topography used to calculate the topography spectrum function. The atmospheric response function was calculated at each point that the spectrum function was calculated. The integrals for the two components of the stress are

$$\overline{\rho u w} = 2\rho(0) \int_{0}^{k_c} \int_{-l_c}^{l_c} U_n^2(0) \; A(k,l) \; F(k,l) \; k\,dk\,dl \qquad (2.3)$$

and

$$\overline{\rho v w} = 2\rho(0) \int_{0}^{k_c} \int_{-l_c}^{l_c} U_n^2(0) \; A(k,l) \; F(k,l) \; l\,dk\,dl \qquad (2.4)$$

where the limits of integration in wavenumber space are determined by the resolution of the topography.

Our purpose in studying the stress integral was to re-
duce the number of calculations of the atmospheric response
function required to calculate the stress.

A reduction of the time required to solve the Scorer
equation will not, by itself, simplify the wave drag calcula-
tion to the extent necessary to meet the requirements of the
GCM. The actual computing time that can be devoted to the
calculation of the wave drag in the GCM will depend upon the
persistence of the wave drag and the number of cycles that
will not require a recalculation of the drag. We have found
that the wave drag is on the order of 6 to 7 dynes/cm$^2$ on a
4° by 5° grid with the northwest corner located at 121°W 37°N.
If an upper limit of 10 dynes/cm$^2$ is taken and we assume that
all of the momentum is taken out of the lower layer of the GCM
(typically 3 km in depth) then the change in the wind speed in
the lower layer will be on the order of 1 m/sec/hour of appli-
cation of this stress. The meridional component of the wind
velocity is typically 5 to 10 m/sec in the lower layer, hence
the wave drag should be recalculated at least every hour in
the GCM. Further studies of the persistence of the drag will
be performed on the final version of the wave drag subroutine.

The running time for older versions of the GCM is
typically 17 min of computer time per day of calculation. If
we increase this running time by 5% for the initial parameteri-
zation then 2 sec of computing time will be available for each
calculation if the calculation is performed once in an hour.
Our calculations have shown that the magnitude of the stress
will only be significant when large mountains are present in a
GCM grid. We have specified the grids that will require a
calculation of the wave drag in Figure 14. There are on the
order of 400 of these grids. With 2 sec of computing time
available for each cycle, we can use $5 \times 10^{-3}$ sec to compute
the drag for each grid.

31
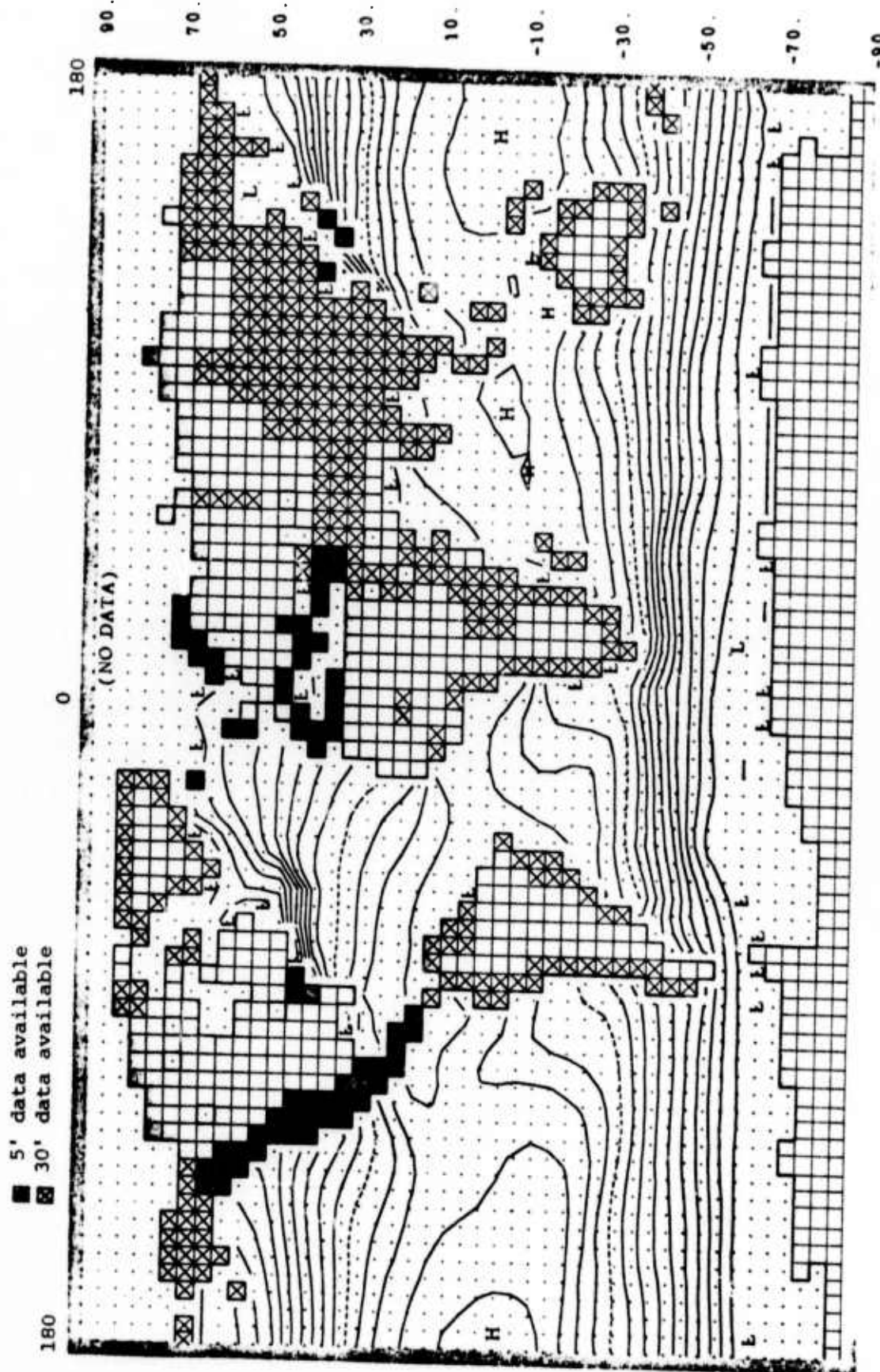
Figure 14. The topography grids containing the mountainous terrain around the world. See text in Section 3 for further clarification of the location of these grids.

32

To utilize the resolution of our 5' topography data to the fullest on the GCM 4° by 5° grids, a 64 by 64 grid is required (the fast Fourier transform requires the number of grids to be powers of 2). The symmetry properties of the atmospheric response function and the topography spectrum function, which were discussed in the previous semiannual report,[8] reduce the number of grids required for the calculation of the stress integrals to 32 by 64. The simplest analytic solution of the Scorer equation is the sinusoidal solution. The sine function and the cosine function require approximately 30 sec of computing time on the UCLA 360/91. In a two-level model approximately 10 calculations of the sine or cosine function are required for each wavenumber component of the stress. Hence, with the simplest analytic model fewer than 16 solutions of the Scorer equation can be obtained for the calculation of the two components of the stress.

The first task that was completed after the development of the stress integral code was to calculate the stress integrals for a series of topography grids. Two atmospheres were chosen from a run of the Rand GCM and the stress was calculated over six topography grids. The two atmospheres are listed as atmospheres 1 and 2 in Table 2. The first five topography grids and the last grid listed in Table 1 were involved in the calculation. The component of the drag in the direction of the zonal wind has been illustrated in Figure 15 for atmosphere 1. The results of the drag calculation for the other component of the stress and the two components for the other atmosphere are tabulated in Table 3. The westernmost grid includes the Coast Range, the San Joaquin Valley and parts of the Sierra Nevada range. It is a grid with extreme variations in height. The next grid includes parts of the Sierra Nevadas and Death Valley. The easternmost edge of TOPO5 is just west of the San Juan Mountains and the Sangre de Cristo Mountains in New Mexico. The grids represented by TOPO4 and

33
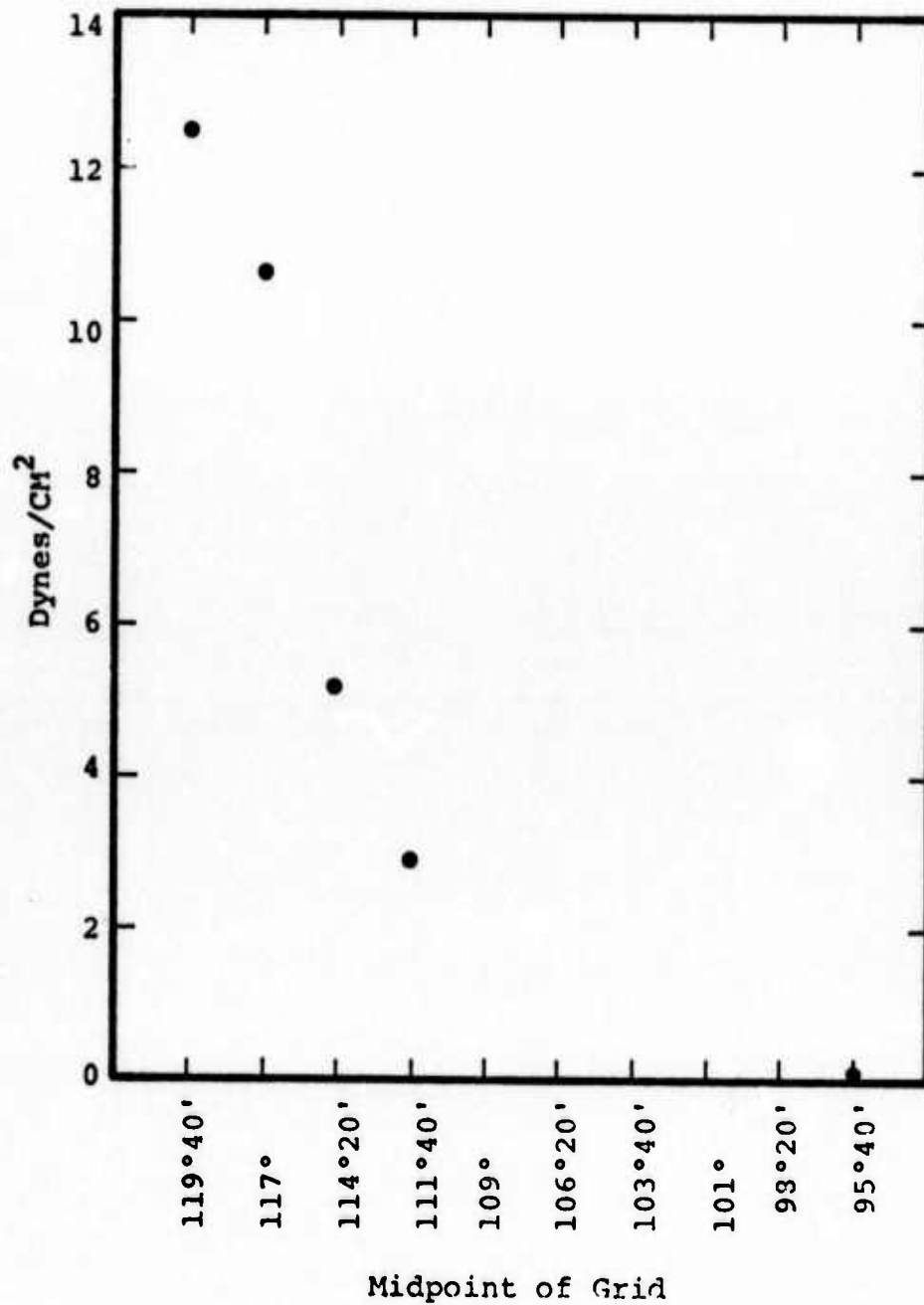
Figure 15.  The wavedrag as a function of the topography grid
for atmosphere 1.

TABLE 3
THE RESULTS OF THE STRESS PARAMETERIZATION

| ATMOSPHERE LOCATION | ZONAL STRESS | MERIDIONAL STRESS | $\rho uw/\rho kA$ | $\rho vw/\rho|\ell|A$ | $\dfrac{(\rho uw)(\rho|\ell|A)}{(\rho vw)(\rho kA)}$ |
|---|---|---|---|---|---|
| Atmosphere 1 | | | | | |
| Topography 1 | -12.5 | 4.22 | -0.0968 | 0.0656 | -1.48 |
| Topography 2 | -10.6 | 4.13 | -0.112 | | |
| Topography 3 | - 5.18 | 1.38 | -0.0953 | | |
| Topography 4 | - 2.95 | 1.52 | -0.113 | | |
| Topography 5 | - 1.40 | 0.596 | -0.11 | | |
| | | | | | |
| Atmosphere 2 | - 0.061 | 0.0294 | -0.0795 | 0.039 | -2.06 |
| Topography 1 | 13.96 | -5.83 | 0.107 | 0.0908 | 1.18 |
| Topography 2 | 11.62 | -5.59 | 0.122 | | |
| Topography 3 | 5.77 | -3.13 | 0.106 | | |
| Topography 4 | 2.69 | -2.18 | 0.103 | | |
| Topography 5 | 1.39 | -0.92 | 0.109 | | |
| | | | | | |
| Atmosphere 3 | | | | | |
| Topography 1 | -12.38 | 4.15 | -0.096 | 0.0646 | -1.48 |
| Topography 2 | -10.39 | 4.17 | -0.109 | | |
| | | | | | |
| Atmosphere 4 | | | | | |
| Topography 1 | -11.50 | 4.70 | -0.089 | 0.0731 | -1.22 |
| Topography 2 | - 8.54 | 3.84 | -0.090 | | |
| | | | | | |
| Atmosphere 5 | | | | | |
| Topography 1 | 14.90 | -5.28 | 0.115 | -0.082 | 1.40 |
| | | | | | |
| Atmosphere 6 | | | | | |
| Topography 1 | 13.37 | -5.20 | 0.103 | -0.081 | -1.27 |
| | | | | | |
| Atmosphere 7 | | | | | |
| Topography 1 | 15.74 | -5.57 | 0.121 | 0.087 | 1.39 |
| | | | | | |
| Atmosphere 8 | | | | | |
| Topography 1 | 8.90 | -5.08 | 0.0687 | -0.0791 | 0.87 |
| | | | | | |
| Atmosphere 9 | | | | | |
| Topography 1 | 15.78 | -6.27 | 0.122 | -0.097 | -1.26 |
| | | | | | |
| Atmosphere 10 | | | | | |
| Topography 1 | - 4.27 | -5.30 | 0.033 | -0.082 | -0.402 |

35

TABLE 3, continued

| ATMOSPHERE LOCATION | ZONAL STRESS | MERIDIONAL STRESS | $\rho uw/\rho kA$ | $\rho vw/\rho\|\ell\|A$ | $\dfrac{(\rho uw)(\rho\|\ell\|A)}{(\rho vw)(\rho kA)}$ |
|---|---|---|---|---|---|
| Atmosphere 11 Topography 1 | 13.35 | 1.10 | 0.103 | 0.017 | 6.06 |
| Atmosphere 12 Topography 1 | -11.12 | -2.74 | -0.086 | -0.043 | 2.0 |
| Atmosphere 13 Topography 1 | 7.1 | -2.98 | 0.055 | -0.046 | 1.20 |
| Atmosphere 14 Topography 1 | 7.73 | -0.48 | 0.060 | $-7.4\times10^{-3}$ | 8.1 |
| Atmosphere 15 Topography 1 | 2.80 | -1.37 | 0.022 | -0.021 | 1.05 |

TOPO5 are south of the very rugged region of the Rockies in Utah and Colorado. The last grid, TOPO10, contains sections of Arkansas and Oklahoma.

The early runs that were made of the copography spectrum function and atmospheric response function indicated that $F(k,l)$ was nearly constant compared with the highly varying spectrum function. It was found that the topography spectrum function was large for small wavenumbers and fell off rapidly as the wavenumbers increased. If the spectrum function is localized in wavenumber space then the product $U_n^2(0) F(k,l)$ should be nearly constant for the wavenumbers which dominate the stress integral. If this is true, then dividing the stress integral in Eq. (2.3) by

$$2\rho(0) \int_0^{k_c} \int_{-l_c}^{l_c} kA(k,l) \, dkdl \qquad (2.5)$$

and the stress integral in Eq. (2.4) by

$$2\rho(0) \int_0^{k_c} \int_{-l_c}^{l_c} |l| A(k,l) \, dkdl \qquad (2.6)$$

should produce a function which is independent of the topography. In Table 3 we have tabulated these functions in the fourth and fifth columns. The first two atmospheres, which were run on the five topographies indicate that the ratio of Eq. (2.3) and Eq. (2.5) has an rms deviation about the mean of 7% although the drag varies by an order of magnitude over the five topographies. On TOPO10 the variation is more significant but this can be attributed to the spectrum function being less localized because there are no significant features in the topography.

37

We had an error in the integration routine for Eq. (2.5) and did not obtain much data on this function for the meridional stress. We suspect that this function will not be as constant for the meridional stress as for the zonal stress because the dominant features of the topography tend to run north-south (with the possible exception of the Himalayas); therefore, the spectrum function on the l-axis and on off-axis points is not as large as the values of the spectrum function along the k-axis when large mountains running north-south are in a grid. Some additional work is required to decide how the parameterization of the meridional component of the stress will be treated.

In Table 4 we have tabulated the wavenumbers which dominate the stress integral. Most of the zonal component of the stress is contributed by the wavenumbers for which $l=0$. In this case $U_n$ becomes the zonal wind component and $F(k,l)$ is essentially constant if the Scorer parameter is large.

To simplify the calculation of the stress it would be desirable to store the integral in Eq. (2.4) for each grid and calculate a single value of $U_n^2 F$ for each atmosphere. In Table 5 we have tabulated the calculated value of $U_n^2 F$ for each of the atmospheres that we have considered for the wave-number $(5.21 \times 10^{-5}, 0)$. We have also formed the product of $U_n^2 F$ with the integral in Eq. (2.4) and have compared it with the calculated stress. For most of the atmospheres tabulated the ratio of the stress to the product $U_n^2 F \rho k A$ is between 1.3 and 2.5. Hence, at least for the meridional component of the stress it appears that the wave drag can be calculated to within approximately 30% by calculating the atmospheric response function for a single wavenumber.

We have also tabulated, for some of the atmospheres, the momentum flux which is dissipated at critical layers in

## TABLE 4
### THE MAGNITUDE OF $U_n^2 F$ FOR THE WAVEVECTORS WHICH DOMINATE THE STRESS INTEGRAL
(All units are CGS)

a. Atmosphere 5, Topography 1

| $(k,l)$ | $l^2(H)$ | $l^2(0)$ | $U_n^2(0)$ | H | $U_n^2 F$ | $U_n^2 AFk$ |
|---|---|---|---|---|---|---|
| $(2.6 \times 10^{-7},\ 2.1 \times 10^{-7})$ | $1.03 \times 10^{-10}$ | $5.71 \times 10^{-10}$ | $2.95 \times 10^{5}$ | $1.34 \times 10^{6}$ | 3.87 | 0.23 |
| $(5.2 \times 10^{-7},\ -4.2 \times 10^{-7})$ | $1.03 \times 10^{-10}$ | $5.71 \times 10^{-10}$ | $2.95 \times 10^{5}$ | $1.34 \times 10^{6}$ | 3.88 | 1.19 |
| $(2.6 \times 10^{-7},\ 0)$ | $5.15 \times 10^{-11}$ | $1.11 \times 10^{-7}$ | $1.52 \times 10^{-5}$ | $1.34 \times 10^{6}$ | 8.31 | 2.56 |
| $(5.2 \times 10^{-7},\ 0)$ | $5.15 \times 10^{-11}$ | $1.11 \times 10^{-7}$ | $1.52 \times 10^{-5}$ | $1.34 \times 10^{6}$ | 8.37 | 2.71 |
| $(7.8 \times 10^{-7},\ 0)$ | $5.15 \times 10^{-11}$ | $1.11 \times 10^{-7}$ | $1.52 \times 10^{-5}$ | $1.34 \times 10^{6}$ | 8.43 | 1.77 |
| $(1.0 \times 10^{-6},\ 0)$ | $5.15 \times 10^{-11}$ | $1.11 \times 10^{-7}$ | $1.52 \times 10^{-5}$ | $1.34 \times 10^{6}$ | 8.45 | 1.43 |
| $(1.3 \times 10^{-6},\ 0)$ | $5.15 \times 10^{-11}$ | $1.11 \times 10^{-7}$ | $1.52 \times 10^{-5}$ | $1.34 \times 10^{6}$ | 8.34 | 0.84 |
| $(1.6 \times 10^{-6},\ 0)$ | $5.15 \times 10^{-11}$ | $1.11 \times 10^{-7}$ | $1.52 \times 10^{-5}$ | $1.34 \times 10^{6}$ | 7.96 | 0.39 |

Total drag in these wavenumbers                                      11.12

TOTAL WAVE DRAG  =  14.9 dynes/cm$^2$

39

TABLE 4, continued

b. Atmosphere 11, Topography 1

| $(k,l)$ | $l^2(H)$ | $l^2(0)$ | $U^2_n(0)$ | H | $U^2_nF$ | $U^2_nAFk$ |
|---|---|---|---|---|---|---|
| $(2.6\times10^{-7}, 2.1\times10^{-7})$ | $7.57\times10^{-11}$ | $5.6\times10^{-9}$ | $2.64\times10^{4}$ | $1.42\times10^{5}$ | 2.60 | 0.80 |
| $(2.6\times10^{-7}, 0)$ | $4.83\times10^{-11}$ | $1.14\times10^{-9}$ | $1.32\times10^{5}$ | $1.42\times10^{6}$ | 7.76 | 2.39 |
| $(5.2\times10^{-7}, 0)$ | $4.83\times10^{-11}$ | $1.14\times10^{-9}$ | $1.32\times10^{5}$ | $1.42\times10^{6}$ | 7.86 | 2.55 |
| $(7.8\times10^{-7}, 0)$ | $4.83\times10^{-11}$ | $1.14\times10^{-9}$ | $1.32\times10^{5}$ | $1.42\times10^{6}$ | 7.99 | 1.68 |
| $(1.0\times10^{-6}, 0)$ | $4.83\times10^{-11}$ | $1.14\times10^{-9}$ | $1.32\times10^{5}$ | $1.42\times10^{6}$ | 8.06 | 1.36 |
| $(1.3\times10^{-6}, 0)$ | $4.83\times10^{-11}$ | $1.14\times10^{-9}$ | $1.32\times10^{5}$ | $1.42\times10^{6}$ | 7.96 | 0.80 |
| $(1.6\times10^{-6}, 0)$ | $4.83\times10^{-11}$ | $1.14\times10^{-9}$ | $1.32\times10^{5}$ | $1.42\times10^{6}$ | 7.49 | 0.37 |

Total drag in these wavenumbers    9.95

TOTAL DRAG = 13.3 dynes/cm$^2$

TABLE 4, continued

c. Atmosphere 12, Topography 1

| $(k,l)$ | $l^2(H)$ | $l^2(0)$ | $U_n^2(0)$ | H | $U_n^2F$ | $U_n^2AFk$ |
|---|---|---|---|---|---|---|
| $(2.6 \times 10^{-7}, 2.1 \times 10^{-7})$ | $2.89 \times 10^{-8}$ | $7.74 \times 10^{-9}$ | $1.90 \times 10^4$ | $1.42 \times 10^4$ | $-3.75$ | $-1.15$ |
| $(5.2 \times 10^{-7}, -4.2 \times 10^{-7})$ | $2.89 \times 10^{-8}$ | $7.74 \times 10^{-9}$ | $1.90 \times 10^4$ | $1.42 \times 10^4$ | $-3.75$ | $-0.22$ |
| $(2.6 \times 10^{-7}, 0)$ | $3.06 \times 10^{-4}$ | $6.02 \times 10^{-10}$ | $2.39 \times 10^5$ | $5.68 \times 10^4$ | $-4.53$ | $-1.40$ |
| $(5.2 \times 10^{-7}, 0)$ | $3.06 \times 10^{-4}$ | $6.02 \times 10^{-10}$ | $2.39 \times 10^5$ | $5.68 \times 10^4$ | $-4.53$ | $-1.47$ |
| $(7.8 \times 10^{-7}, 0)$ | $3.06 \times 10^{-4}$ | $6.02 \times 10^{-10}$ | $2.39 \times 10^5$ | $5.68 \times 10^4$ | $-4.53$ | $-0.95$ |
| $(1.0 \times 10^{-6}, 0)$ | $3.06 \times 10^{-4}$ | $6.02 \times 10^{-10}$ | $2.39 \times 10^5$ | $5.68 \times 10^4$ | $-4.53$ | $-0.77$ |
| $(1.3 \times 10^{-6}, 0)$ | $3.06 \times 10^{-4}$ | $6.02 \times 10^{-10}$ | $2.39 \times 10^5$ | $5.68 \times 10^4$ | $-4.53$ | $-0.46$ |
| $(1.6 \times 10^{-6}, 0)$ | $3.06 \times 10^{-4}$ | $6.02 \times 10^{-10}$ | $2.39 \times 10^5$ | $5.68 \times 10^4$ | $-4.53$ | $-0.22$ |

Total drag in these wavenumbers  $-6.63$

TOTAL DRAG $= 11.12$ dynes/cm$^2$

41

## TABLE 5
## ANALYSIS OF TREATING $U_n^2F$ TO BE A CONSTANT VALUE

| ATMOSPHERE LOCATION | (k,l) | $U_n^2F(k,l)$ | $U_n^2F(\overline{\rho k A})$ | $\rho uw$ | $\dfrac{\rho uw}{[U_n^2 F \rho k A]}$ |
|---|---|---|---|---|---|
| Atmosphere 1 | | | | | |
| Topography 1 | $(2.6\times10^{-7},\ 2.1\times10^{-7})$ | -4.53 | - 5.9 | -12.54 | 2.12 |
| Topography 2 | | -4.53 | - 4.3 | -10.68 | 2.48 |
| Topography 3 | | -4.53 | - 2.46 | - 5.18 | 2.10 |
| Topography 4 | | -4.53 | - 1.19 | - 2.96 | 2.48 |
| Topography 5 | | -4.53 | - 0.58 | - 1.40 | 2.41 |
| Topography 10 | | -4.53 | - 0.035 | - 0.061 | 1.74 |
| Atmosphere 2 | | | | | |
| Topography 1 | | 7.76 | 10.1 | 13.96 | 1.38 |
| Topography 2 | | 7.76 | 7.38 | 11.61 | 1.57 |
| Topography 3 | | 7.76 | 4.22 | 5.77 | 1.37 |
| Topography 4 | | 7.76 | 2.04 | 2.69 | 1.32 |
| Topography 5 | | 7.76 | 1.00 | 1.39 | 1.39 |
| Atmosphere 3 | | | | | |
| Topography 1 | | -4.55 | - 5.91 | -12.38 | 2.10 |
| Topography 2 | | -4.55 | - 4.31 | -10.39 | 2.41 |
| Atmosphere 4 | | | | | |
| Topography 1 | | -3.89 | - 5.05 | -11.50 | 2.28 |
| Topography 2 | | -3.89 | - 3.68 | - 8.54 | 2.32 |
| Atmosphere 5 | | | | | |
| Topography 1 | | 8.37 | 11.0 | 14.9 | 1.35 |
| Atmosphere 6 | | | | | |
| Topography 2 | | 7.00 | 9.1 | 13.4 | 1.47 |

TABLE 5, continued

| ATMOSPHERE LOCATION | (k,l) | $U_n^2F(k,l)$ | $U_n^2F(\overline{\rho kA})$ | $\rho uw$ | $\dfrac{\rho uw}{[U_n^2 F \overline{\rho kA}]}$ |
|---|---|---|---|---|---|
| Atmosphere 7 Topography 1 | $(2.6\times10^{-7}, \ 2.1\times10^{-7})$ | 8.81 | 11.5 | 15.7 | 1.37 |
| Atmosphere 8 Topography 1 | | 3.29 | 4.28 | 8.90 | 2.08 |
| Atmosphere 9 Topography 1 | | 8.05 | 10.5 | 15.78 | 1.50 |
| Atmosphere 10 Topography 1 | | 1.10 | 1.43 | - 4.27 | 2.99 |
| Atmosphere 11 Topography 1 | | 7.86 | 1.43 | - 4.27 | 2.99 |
| Atmosphere 12 Topography 1 | | -4.53 | 10.2 | 13.35 | 1.31 |
| Atmosphere 13 Topography 1 | | 2.98 | 3.87 | 7.10 | 1.83 |
| Atmosphere 14 Topography 1 | | 3.87 | 5.03 | 7.73 | 1.54 |
| Atmosphere 15 Topography 1 | | $9.37\times10^{-1}$ | 1.22 | 2.80 | 2.29 |

the lower layer and that which gets through to the upper layer.
These results are given in Table 6. One of the difficulties
with a two-layer model is deciding where the momentum which
propagates into the stratosphere comes from. We are making
the assumption that since the momentum flux would not be
present in the absence of the mountains that the momentum must
be taken from the lower layer. It is obvious that momentum
will, in fact, be taken from both layers but it is quite diffi-
cult to decide what the contribution is from each layer.

## 3. PARAMETERIZATION OF THE WAVE DRAG

In this section we summarize the progress that has been
made toward delivery of a subroutine to the Rand Corporation
for calculation of the mountain wave drag. We have been de-
layed by the time required to get acquainted with the DARPA
network and approximately six to eight man-weeks of work re-
mains until the subroutine package is completed. Most of the
work has been completed on the parameterization of the zonal
component of the stress. During the next phase of the con-
tract period, we will be determining the number of components
of the meridional stress that can be calculated within the
limitations of the computing time available.

### 3.1 Work That Has Been Completed

In the last section we discussed the work that has been
completed on the simplification of the two components of the
stress. In particular, the zonal stress is apparently suscep-
tible to great simplification over mountainous terrain. We
propose to treat the zonal component of the stress to be inde-
pendent of the meridional wind and to calculate a single at-
mospheric response function for the calculation of the zonal
stress integral. The results given in Table 5 indicate that
this can be done (in particular, see atmosphere 13 and 14).

## TABLE 6
## VERTICAL DISTRIBUTION OF THE MOMENTUM FLUX

| ATMOSPHERE LOCATION | $\overline{\rho uw}$UP | $\overline{\rho uw}$DOWN | $\overline{\rho vw}$UP | $\overline{\rho vw}$DOWN |
|---|---|---|---|---|
| Atmosphere 1 Topography 1 | $1.86 \times 10^{-2}$ | -12.1 | $1.18 \times 10^{-1}$ | 3.99 |
| Atmosphere 2 Topography 10 | $4.28 \times 10^{-4}$ | $-6.13 \times 10^{-2}$ | $2.19 \times 10^{-3}$ | $2.72 \times 10^{-2}$ |
| Atmosphere 5 Topography 1 | 15.1 | $-2.23 \times 10^{-1}$ | -3.0 | -2.28 |
| Atmosphere 6 Topography 1 | 13.63 | $-2.58 \times 10^{-1}$ | -2.84 | -2.36 |
| Atmosphere 7 Topography 1 | 15.89 | $-1.52 \times 10^{-1}$ | -3.39 | -2.18 |
| Atmosphere 8 Topography 1 | 9.21 | $-3.04 \times 10^{-1}$ | -2.64 | -2.44 |
| Atmosphere 9 Topography 1 | 15.92 | $-1.35 \times 10^{-1}$ | -4.14 | -2.13 |
| Atmosphere 10 Topography 1 | 4.72 | $-4.50 \times 10^{-1}$ | -2.64 | -2.66 |
| Atmosphere 11 Topography 1 | 13.38 | $-2.76 \times 10^{-2}$ | $2.63 \times 10^{-1}$ | $8.34 \times 10^{-1}$ |
| Atmosphere 12 Topography 1 | $1.40 \times 10^{-1}$ | -11.26 | $-4.6 \times 10^{-1}$ | -2.28 |
| Atmosphere 13 Topography 1 | 7.10 | $-2.12 \times 10^{-3}$ | -2.97 | $-4.68 \times 10^{-3}$ |
| Atmosphere 14 Topography 1 | 7.65 | $8.09 \times 10^{-2}$ | $-5.89 \times 10^{-1}$ | $1.12 \times 10^{-1}$ |
| Atmosphere 15 Topography 1 | 2.80 | $-1.51 \times 10^{-3}$ | -1.36 | $-3.31 \times 10^{-3}$ |

The zonal component of the stress will be determined for each grid where we anticipate wave drag to be important. The atmospheric response function will be calculated analytically for a single wavenumber on the k-axis in wavenumber space and multiplied by the square of the ground level zonal winds. This product will be multiplied by the integral

$$\int_0^{k_c} \int_{-l_c}^{l_c} kA(k,l) \, dkdl \tag{3.1}$$

which will be available in core storage for each grid to be used and a constant factor which our results to date indicate should be approximately 1.9.

The flow diagram of the subroutine for the calculation of the zonal stress is shown in Figure 16. For this initial determination of the relative magnitude of the wave drag we are developing a two-level model of the Scorer parameter. In this model constant values of the Scorer parameter are taken for each level of the GCM. The Scorer parameter in the upper level of the GCM is determined by the wind speed and the temperature at $\sigma = 3/4$. The lapse rate is determined by the temperatures and geopotentials at the $\sigma = 1/2$ and $\sigma = 1$ levels. Similarly, the Scorer parameter can be calculated for the lower level. The assumption of a constant Scorer parameter in each layer allows the simplest analytic solution to the Scorer equation to be used. The initialization of the solution occurs at the 200 mb level or at a level where a critical layer occurs. When $l^2(H) > \kappa^2$ the solution of the Scorer equation is sinusoidal and we take the solution for outward propagating waves. In the case where $l^2(H) < \kappa^2$ the wave should be considered a part of the discrete spectrum. However, in general,
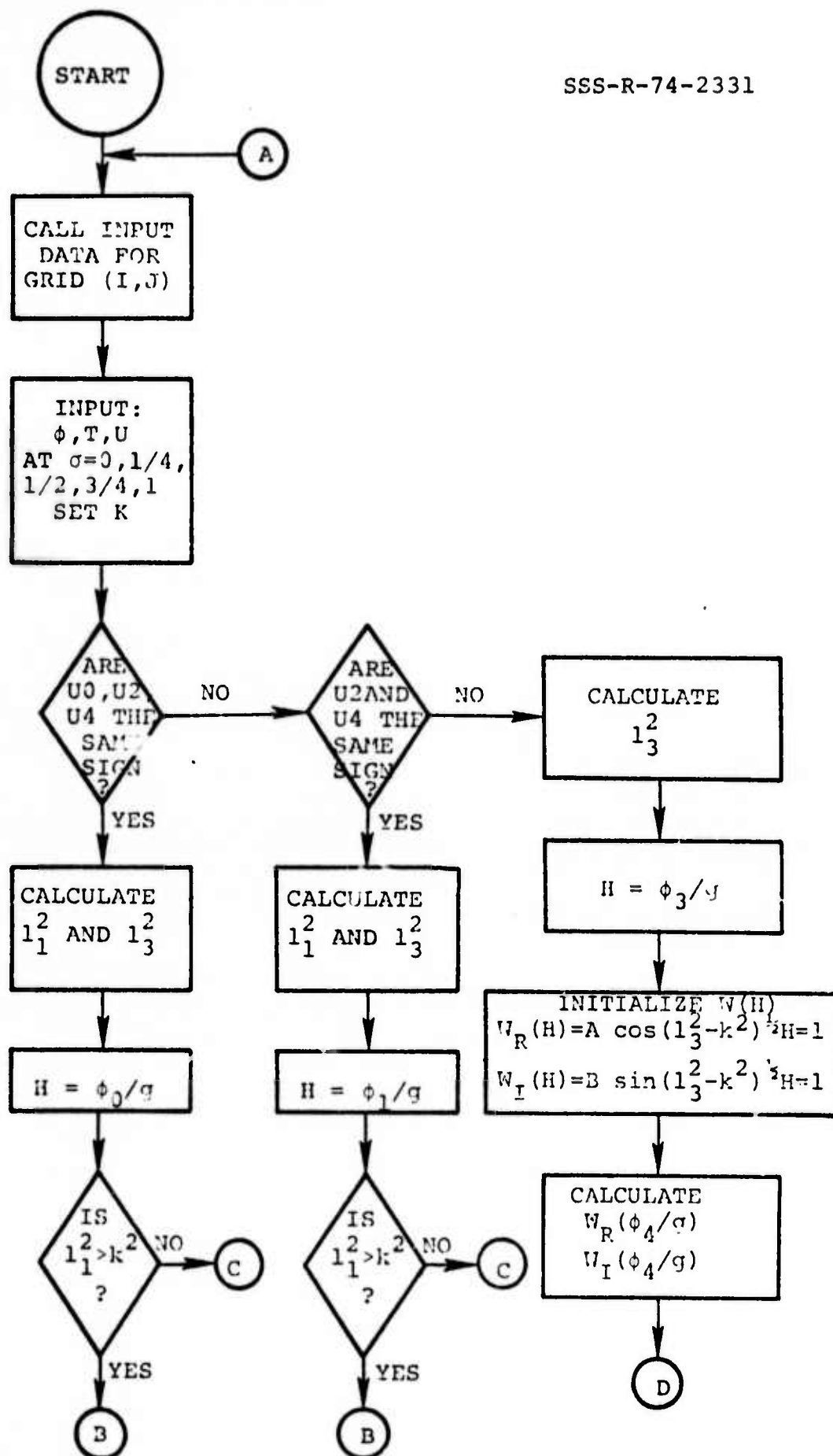
46

Figure 16. Flow diagram for the calculation of the zonal component of the stress.
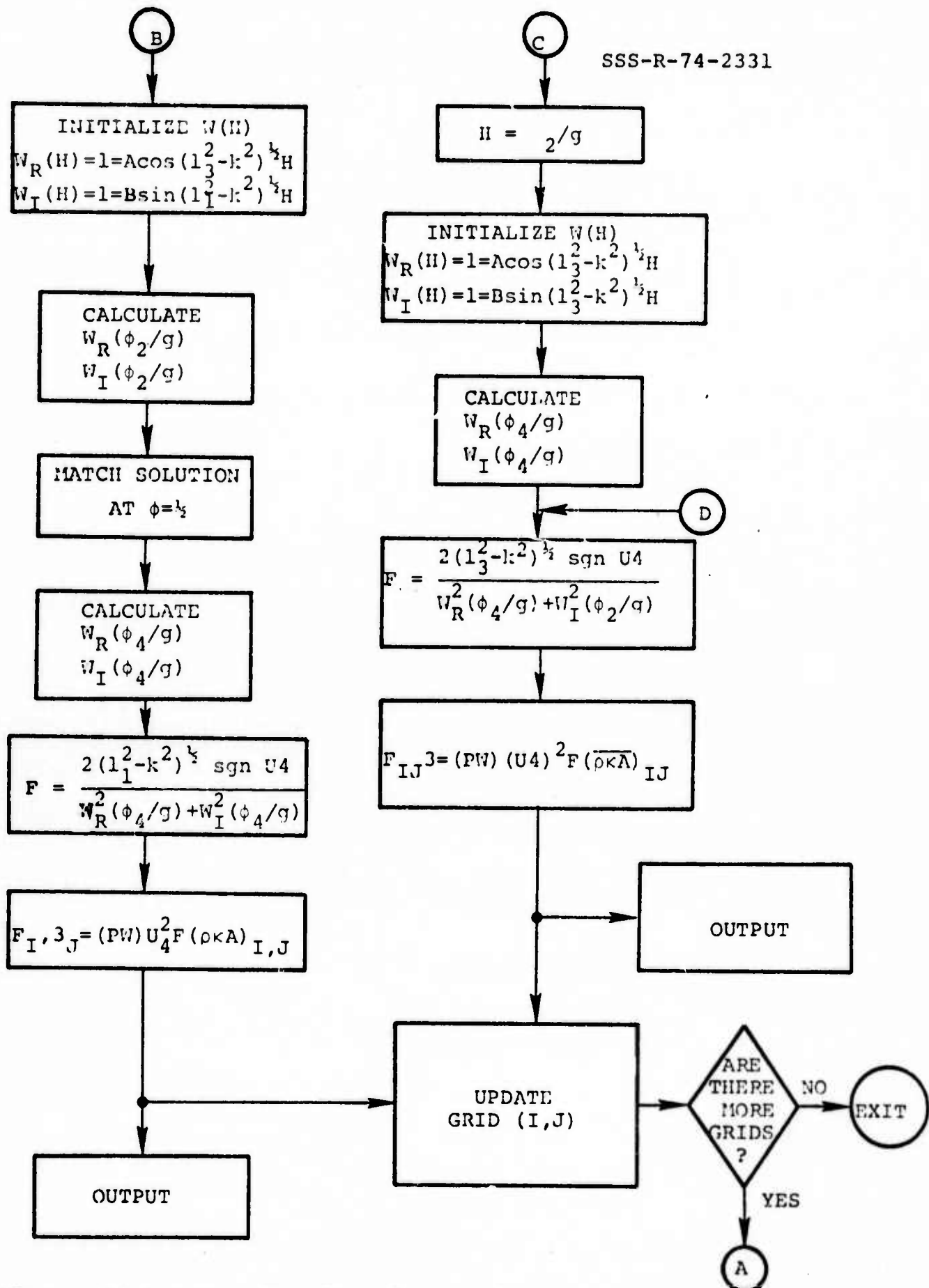
B

INITIALIZE W(H)
$W_R(H) = 1 = A\cos(l_3^2 - k^2)^{\frac{1}{2}} H$
$W_I(H) = 1 = B\sin(l_1^2 - k^2)^{\frac{1}{2}} H$

CALCULATE
$W_R(\phi_2/g)$
$W_I(\phi_2/g)$

MATCH SOLUTION
AT $\phi = \frac{1}{2}$

CALCULATE
$W_R(\phi_4/g)$
$W_I(\phi_4/g)$

$F = \dfrac{2(l_1^2 - k^2)^{\frac{1}{2}} \operatorname{sgn} U4}{W_R^2(\phi_4/g) + W_I^2(\phi_4/g)}$

$F_{I,3J} = (PW) U_4^2 F(\rho\kappa A)_{I,J}$

OUTPUT

C

$H = {}_2/g$

INITIALIZE W(H)
$W_R(H) = 1 = A\cos(l_3^2 - k^2)^{\frac{1}{2}} H$
$W_I(H) = 1 = B\sin(l_3^2 - k^2)^{\frac{1}{2}} H$

CALCULATE
$W_R(\phi_4/g)$
$W_I(\phi_4/g)$

D

$F = \dfrac{2(l_3^2 - k^2)^{\frac{1}{2}} \operatorname{sgn} U4}{W_R^2(\phi_4/g) + W_I^2(\phi_2/g)}$

$F_{IJ}3 = (PW)(U4)^2 F(\overline{\rho\kappa A})_{IJ}$

OUTPUT

UPDATE
GRID (I,J)

ARE THERE MORE GRIDS ? → NO → EXIT

YES

A

Figure 16 (continued).   Flow diagram for the calculation of the
zonal compenent of the stress.

48

the trapped wave spectrum will contribute little to the total
drag and for simplicity of the calculation the integration is
started at the level for which $1^2(H) > \kappa^2$ .

For outward propagating waves, the real solution of the
Scorer equation is

$$w_R = A \cos[(1^2(z) - \kappa^2)z] \qquad (3.2)$$

and the imaginary solution is

$$w_I = B \sin[(1^2(z) - \kappa^2)z] \quad . \qquad (3.3)$$

The boundary conditions applied at $z=H$ are $w_R=w_I=1$ , cor-
responding to one unit of kinetic energy arriving at this
level.  The solution corresponding to this boundary condition
is found at the $\sigma = 1/2$ level if $z=H$ occurs above the
$\sigma = 1/2$ level and is then matched to the corresponding solu-
tion in the lower level.  Finally the solution at the ground
level is obtained and the ospheric response function,

$$F(k,1) = \frac{2(1^2(H) - \kappa^2)^{1/2}}{w_R^2 + w_I^2} \qquad (3.4)$$

is evaluated.  Here, $w_R$ and $w_I$ are calculated at $\sigma = 1$ .
The ground level winds are obtained from the GCM.  The product
of Eqs. (3.1) and (3.4), the ground level zonal component of
the wind, and the parameterized correction value give the zonal
stress.

The two level model described above was used by Palm
and Foldvik,[9] with a third level above specifying an expo-
nentially decaying Scorer parameter.  A third analytic solu-
tion to the Scorer equation was given by Vergeiner.[10]  We

49

have considered applying the Vergeiner solution to a two-level model with a constant stability and the wind profile that is used to extrapolate the two-level winds in the GCM (essentially exponential in z). The additional computing time required to determine the two parameters and to match the solutions at the $\sigma = 1/2$ level will only be justified if the Scorer parameter used by Vergeiner closely approximates the true atmospheric Scorer parameter. If the actual Scorer parameter profile is denoted by $l_A^2(z)$ and the profile which gives an analytic solution over an atmosphere of depth $\Delta z$ is denoted by $l_s^2(z)$ then the condition for the atmospheric response to be nearly the same for the two profiles is

$$\int_{z_1}^{z_2} \left| [l_A^2(z) - \kappa^2]^{1/2} - [l_s^2(z) - \kappa^2]^{1/2} \right| ds \ll \frac{\pi}{2} \ , \quad (3.5)$$

where $\Delta z = z_2 - z_1$ . When the actual atmosphere was formulated in terms of the wind profile given in the GCM, Eq. (3.5) could not be satisfied with a two-level model employing the Vergeiner solution for the two levels. Therefore, the decision was made to use the simpler prescription for the Scorer parameter.

In Table 6 we have tabulated the vertical distribution of the momentum flux for the atmospheres that were studied. In general, the zonal component of the wind was large in the upper layer and very little of the momentum was dissipated in this layer. For many of the atmospheres, critical layers accounted for the dissipation of very little of the momentum flux, and the majority of the momentum deficit in the troposphere propagated into the stratosphere (most of the flux listed under $\overline{\rho u w u p}$). In the present model the momentum flux which is not dissipated in the troposphere is treated as a deficit in the lower layer. In reality there is an exchange of momentum in

both layers and there should be momentum taken out of both layers of the GCM. We have discussed this question in depth with people working in the field without a satisfactory solution. This is a fallacy of the linear, inviscid model which will require an investigation of the results of incorporating our subroutine into the GCM.

The output of the wave drag subroutine will be two forces, each to be applied to one of the two levels of the GCM. The components of the two forces will act against the meridional and zonal components of the wind. We have discussed the persistence of these forces in terms of the effect these forces have on the wind components at the two levels. A study will be made in cooperation with Mike Schlesinger and Larry Gates at Rand to determine the persistence of the drag in terms of the other forces acting on the windfield prior to the incorporation of the wave drag subroutine into the GCM.

We have completed the transfer of the topography tapes up to UCLA. These tapes have been properly formatted and the code has been developed for calculating the topography spectrum function, and subsequently, Eq. (3.1) for each grid. We have discovered gaps in the 5' data in those regions specified in Figure 14. Time will not permit a thorough inspection and re-structuring of these tapes; therefore, we will be using only the 30' data for all the grids specified in Figure 14 on our initial run in the GCM.

There is an additional error in the grids shown in Figure 14. We have drawn the relevant topography grids on the matrix of grids used in the GCM. These grids have the velocity points on the edges and the scalar variables at the center of the grid. We will actually be performing our calculations on grids centered on velocity points and will require four point averages of the scalar variables for each grid. Therefore,

the actual topography grids that will be used are centered 2°
to the north and 2°30' to the west of those grids shown in
Figure 14.

## 3.2  Work to be Completed in this Contract Period

In order to complete the parameterization of the wave
drag a series of tasks are to be completed in the next two
months.  The final task of the contract will be the delivery of
the subroutine to Rand for testing and incorporation into the
GCM.

### 3.2.1  Additional Runs of the Meridional Stress -- The first
task is being undertaken at this time.  Additional runs of the
stress integral are being made to determine to what degree the
meridional stress can be simplified.  We do not expect to be
able to calculate a single component of the stress as we are
able to do with the zonal component.  However, the simplifica-
tion that has been found in the zonal stress will provide addi-
tional computing time for the meridional stress and should
allow the calculation of the atmospheric response function for
ten to 15 wavenumbers.

### 3.2.2  Coding of the Analytic Solutions -- The coding of the
analytic solutions will follow a flow diagram similar to that
shown in Figure 16.  In addition, it will contain a loop that
will provide for a calculation of the atmospheric response
function for a variable number of wavenumbers.

### 3.2.3  Determination of the Number of Wavenumbers Used in the
Meridional Stress Calculation -- The third task will include a
series of timing runs to determine how many of the components
of the stress integral can be calculated in the time allotted.

3.2.4  Calculate the Spectrum Function for the Important Points
-- The spectrum function will be calculated and stored for
those wavenumbers which will enter the meridional stress calcu-
lation.  As we have stated previously, the topography will be
resolved to 30' for this initial run and only those grids
designated in Figure 14 will be used.  The codes to calculate
the spectrum function have been developed and are operational.

3.2 5  Final Version of the Subroutine -- After the completion
of the above tasks, the final version of the subroutine will
be written.  For this initial test on the GCM, the subroutine
will be designed to add less than 5% to the running time of the
global circulation model.  The 5% figure will be based on a
recalculation of the drag every hour, and the actual increase
in run time will depend on the persistence tests to be run by
Rand.

The code will provide forces in mks units to be applied
for the time specified by Rand.

3.3  Subsequent Work on the Wave Drag Subroutine

We do not believe that the wave drag subroutine will
have been adequately studied at the end of this contract period.
Some additional work has been discussed in the preceding sec-
tions and we summarize here the work that remains on this pro-
ject.  Much of this work would have been accomplished during
this contract period had we not required the changeover in
computing operations.

3.3.1  Additional Testing of the Parameterization -- The
parameterization that is being developed requires additional
testing on topographies that differ from those that have been
used.  In particular, we have not adequately investigated the
magnitude of the drag on topography grids other than the few

listed in Table 1.  The lack of funds and time has also re-
stricted the calculations to smaller grids than the 4° by 5°
grids used in the GCM.  To adequately define the parameters
we should perform additional calculations on the larger grids.

We would encourage the investigation of the stress
integrals over the Himalayas where the wave drag will un-
doubtedly be large and the components of the topography spec-
trum function may be vastly different from those investigated
to date.  In addition, the very high winds that are observed
in the GCM runs over the Himalayas may require a treatment of
the discrete wave spectrum not included in the present param-
eterization.

3.3.2  Determination of Dissipation Mechanisms -- Additional
work will be required to determine at what level momentum is
pumped into the waves and what the means for dissipation of
the momentum carried by the waves is.  We have mentioned that
most of the wave momentum is pumped into the very long wave-
lengths which propagate into the stratosphere.  In the present
parameterization this momentum is taken out of the lower level
of the GCM and is not put back into the circulation.  It may
be necessary to investigate the level at which momentum is
removed by experimenting with the change in the circulation
observed in the GCM as this momentum is removed from the two
levels in varying proportions.

Other dissipation mechanisms, not included in the
present prescription, such as the breaking of waves of large
amplitude, should be investigated.

3.3.3  Improvement of the Analytic Treatment -- We have dis-
cussed in some detail the limitations that are placed on the
number of calculations that can be made to determine the drag.

Until we have determined the time required to make the calculation of the meridional component of the wave drag it will be difficult to specify where improvements in the analytic treatment can be made.

## 4. RADIATION IN THE EARTH'S ATMOSPHERE

The major undertakings for the past contract period were, first, to become proficient in the use of the DARPA Network and the IBM 360/91 computer system at UCLA; second, to convert all the atmospheric radiation codes to run on the 360/91 and verify executions of the codes there against corresponding executions on the $S^3$ UNIVAC 1108; and third, to make major modifications to all the codes in preparation for delivery to the Rand Climate Dynamics Group. Much of this work was of a relatively routine nature but was nevertheless time-consuming and was made immeasurably more difficult by our unfamiliarity with the IBM system, by the lack of adequate consulting services at UCLA, and by the frequent system crashes at UCSD (our local host). As a result, only a few ATRAD production runs have been made on substantially new problems. In the following, the work which has been accomplished on each code to be delivered to Rand is discussed, followed by a summary of work which we intend to complete by the close of the contract.

### 4.1 Near-IR Code

The near-IR code is really a stand-alone code (independent of ATRAD) for calculating up-flux and down-flux in an aerosol-free, non-scattering, non-emitting atmosphere. Since neither the scattering nor Planck terms enter the monochromatic radiative transfer equation in this case, a simple analytic solution is possible for the radiative intensity. The down-flux becomes simply an exponential, and the up-flux an integral

over exponentials weighted by the directionally-dependent surface albedo. When these fluxes are integrated over a finite spectral interval, the exponentials are merely replaced by transmission functions. Hence, the calculation has only three non-trivial parts: the LOWTRAN[14] transmission function scheme, Thekaekara's[15] table of the extra-terrestrial solar flux as a function of wavelength, and an angular quadrature for the up-flux. Results from the near-IR code were compared with ATRAD in the last contract report[7] for the $0.9 - 3.8$ μ region of the spectrum and for two model atmospheres (a dry one and a wet one). It was demonstrated in that report that there are serious errors in the Mugge-Möeller parameterization of solar absorption which is used in the Mintz-Arakawa GCM. According to that parameterization, the fractional absorption of the $> 0.9$ μ solar flux due to a vertical absorber amount $u*$ of water vapor along a slant path at zenith angle $\theta$ is

$$A(u*\sec\theta) = \frac{0.189}{(1-f_o)S_o}(u*\sec\theta)^{0.303} \quad .$$

$u*$ is calculated from a pressure-scaled integral of the water vapor density, and $f_0$ is the $< 0.9$ μ fraction of the mean annual extra-terrestrial solar flux $S_o$ (langleys/min). It was furthermore demonstrated that no substantial improvement in this parameterization could be obtained by using different values of the pressure-scaling factor or of any of the constants in the formula. It was suggested that an entirely new formula be devised, one more accurately approximating the predictions of both ATRAD and the near-IR code.

In order that the Rand Climate Dynamics Group have the facility to generate transmission data to which to fit such a new formula, a copy of the near-IR code was delivered to them. Some work was also initiated here to fit the solar-flux-weighted

56

transmission with piecewise rational functions of u* , and
to that end a rational function fitting code was developed.
Because of time pressures to prepare the other radiation codes
for the 360/91, that effort had to be postponed; however, we
are convinced that rational functions, being merely quotients
of polynomials, and hence, computationally fast compared with
power laws, are the best choices for fitting not only the solar
absorption function but also many of the other functions which
must be parameterized in a GCM.  (Tables are also efficient in
terms of execution time, but tend to swell core storage re-
quirements.)  Our rational function fitting code will be made
available to Rand for use in future parameterization work.

## 4.2 Exponential Fitting Tables Code

The exponential fitting tables code generates spectral-
interval-by-spectral-interval tables of exponential-sum fits
to the transmission, for use by ATRAD.  The modifications which
have been made to the code are described below.

First, the old scheme for combining terms with close
exponents in the exponential sum failed when the code was run
on the 360/91.  Analysis of the problem revealed that the
double precision accuracy on the 360/91 was almost two signifi-
cant digits less than the UNIVAC 1108 upon which the code was
developed, and that the scheme (a secant method) was sensitive
to this decreased precision.  Rather than re-formulate the
secant scheme to be stable, however, it was replaced entirely
with a Newton's method iteration which has higher-order con-
vergence than the secant method (although not guaranteed con-
vergence).  The Newton scheme requires many fewer iterations
than the old secant method (generally 3-7 iterations are suffi-
cient) and in running the exponential fitting code on a wide
variety of transmission data no case has even been encountered
where the new Newton scheme failed to converge.  Mathematically,
the object of the scheme is to fit the sum

$$a_i e^{-k_i u^*} + a_{i+1} e^{-k_{i+1} u^*} \quad ,$$

where $k_i$ and $k_{i+1}$ are close (generally within 5% of one another), with a single term

$$ae^{-ku^*} \quad .$$

The fit is required to be a least-squares one, so that the object is to pick $a$ and $k$ to minimize the residual

$$R = \sum_{j=1}^{N} \left[ a_i e^{-k_i u_j^*} + a_{i+1} e^{-k_{i+1} u_j^*} - ae^{-ku_j^*} \right]^2 \quad .$$

The two simultaneous equations to be solved for $a$ and $k$ are then, in the standard least-squares fashion,

$$\frac{\partial R}{\partial a} \equiv f(a,k) = 0$$

$$\frac{\partial R}{\partial k} \equiv g(a,k) = 0 \quad .$$

The first of these equations can be trivially solved for $a$ and used to eliminate $a$ in the second equation, resulting in a single (non-linear) equation in $k$ alone. This foregoes, however, the availability of an excellent initial guess for $a$, namely

$$a_o = a_i + a_{i+1} \quad .$$

Of course, we also have an excellent initial guess for $k$, which is

58

$$k_o = \frac{1}{2}(k_i + k_{i+1}) \quad .$$

But the opportunity to use the symmetric initialization and the advantage of having a free to assume the "best" value in each iteration caused the two-dimensional form of Newton's method to be selected. The equations for this iteration are

$$f(a_n, k_n) + \frac{\partial f}{\partial a}(a_n, k_n)(a_{n+1} - a_n) + \frac{\partial f}{\partial k}(a_n, k_n)(k_{n+1} - k_n) = 0$$

$$g(a_n, k_n) + \frac{\partial g}{\partial a}(a_n, k_n)(a_{n+1} - a_n) + \frac{\partial g}{\partial k}(a_n, k_n)(k_{n+1} - k_n) = 0 \quad .$$

The second group of code changes concern the selection of the array of transmission function data to be fitted in each spectral interval. Allowance has been made for fitting sections of a transmission curve (between absorber-amounts $u^*_{min}$ and $u^*_{max}$). This is useful for scoping down on parts of transmission curves. The algorithm for selecting the array of transmission data $T_{\Delta\nu}(u^*_j)$ then proceeds as follows:

(1) If $T_{\Delta\nu}(u^*_{max}) > T_{max}$ , do not do fitting.

(2) Otherwise, find smallest $n \geq 0$ such that
$$T_{\Delta\nu}(u^*_{min} + 0.97^n (u^*_{max} - u^*_{min})) \geq T_{min}$$

and let fitting interval be $[u^*_{min}, U]$ , where
$$U \equiv u^*_{min} + 0.97^n (u^*_{max} - u^*_{min}) \quad .$$

(3) Find smallest $N \epsilon [N_{min}, N_{max}]$ such that
$$T_{\Delta\nu}(u^*_{min}) - T_{\Delta\nu}(u^*_{min} + \frac{U - u^*_{min}}{N - 1}) < T_{diff}$$
(if impossible to satisfy this criterion, take $N = N_{max}$) .

59

(4)   The set of transmission data is then

$$T_{\Delta\nu}(u^*_{min} + (j-1)\frac{U-u^*_{min}}{N-1}) \qquad j=1, \ldots, N \, .$$

In the discussion of this algorithm, typical values of the parameters are given in parentheses. Step (1) skips fitting when the atmosphere is essentially transparent ($T_{max}$ = 0.99). Step (2) assures that the smallest transmission value fitted will be larger than $T_{min}$ ($T_{min}$ = 0.005). The choice of $T_{min}$ should be guided by the fact that the LOWTRAN transmissions are truncated to zero below 0.001. Step (3) attempts to keep the difference between the first and second transmission values less than $T_{diff}$ ($T_{diff}$ = 0.01 - 0.02, $N_{min}$ = 5, $N_{max}$ = 101). Since the transmission curve becomes less and less steep as $u^*$ increases, $T_{diff}$ will then (if the step is successful) be the largest difference between any two transmission values. In the centers of strong absorption bands, step (3) is usually unsuccessful and in extreme cases the difference between the first two transmission values is as large as 0.5. This is an inherent limitation in the fitting algorithm, and has two causes. First, because of round-off error accumulation, the algorithm can only fit a finite number of data points (no more than 125-150 with standard double precision arithmetic). Second, the algorithm requires data at equal steps in $u^*$ in order to solve the linear least-squares problem for the coefficients of the exponential sum in a well-conditioned way. Thus, there are generally too many data points for large $u^*$, where the transmission varies slowly, and too few for small $u^*$, where it varies rapidly. In order to get around the equal-steps-of-$u^*$ limitation, it would be necessary to devise a general least-squares algorithm for the coefficients of an arbitrary sum of exponentials. Unfortunately, the latter is a classical ill-conditioned problem of numerical analysis (stemming from the fact that the exponentials form a non-orthogonal set).

The third set of code-changes were directed towards the output formats of the code. The code has two forms of output: first, the exponential fitting parameters for use by ATRAD are directed to a (card-image form) table; second, there are prints of the input parameters, the transmission function data fitted, the corresponding exponential fit and percent error, the coefficients and exponents of the fit, and a summary of each iteration in the fitting process if desired.

Two different forms for the tabular output have been tried. The first dumps all the fitting parameters en masse (into a namelist output format, although this is obviously not essential). The table is then read all at once at the beginning of ATRAD. The advantage of this is that only one ATRAD I/O swap-out is necessary; the disadvantage is that tables of this form are not easily extended (since they are read into arrays of fixed dimension) nor can they be easily altered or even scanned without an interpretive program. The other tabular form dumps the fitting parameters spectral-interval-by-spectral-interval as they are calculated, into a readable card-image-type format. Such tables require several I/O requests by ATRAD for each spectral interval, but offer the advantage of easy extensibility, alterability, and readability. As representative CPU time requirements for ATRAD in the two cases, we offer the following numbers from a clear-sky full-spectrum ATRAD run for a typical tropical atmosphere for 10 sun angles: for the "en masse" tables, 113 CPU seconds (UCLA IBM 360/91); for the interval by interval tables, 175 CPU seconds. There is roughly a 50% penalty in CPU time for using the more flexible table format. When clouds are introduced and Mie tables must also be read and processed, this percentage penalty will, of course, be reduced substantially.

The printed output has been made considerably more readable, particularly the prints of the input variables controlling the calculation. After each input variable is printed

out, its function is now described in detail. This feature (which has also been introduced into the other radiation codes) renders the code much more accessible to inexperienced users.

Two sets of exponential fitting tables were made at UCLA, one for the "normal" ATRAD spectral interval structure used in all ATRAD calculations to date, and one for a very refined spectral interval structure for calculating "benchmark" ATRAD fluxes against which to verify the fluxes predicted with the "normal" spectral interval structure. The "normal" structure, using the notation that $n_1(\Delta n)n_2$ means $n_1, n_1+\Delta n, n_1+2\Delta n,$ ..., $n_2-\Delta n, n_2,$ is (in $cm^{-1}$):

$$60(60)600(20)800(40)1200(80)1600(160)2400(240)4800$$
$$(320)8000(500)32000(1000)35000(1500)48500$$

The refined structure is:

$$60(20)2400(100)11000(200)32000(500)48500$$

The exponential fitting code, printed output from the two production runs ("normal" and refined), and the two fitting tables generated therewith are being delivered to the Rand Climate Dynamics Group.

## 4.3     $i_1+i_2$ Tables Code

This code makes tables of integrals over small ranges $\Delta x$ of size parameter of the fundamental Mie scattering quantities, that is, of

$$\int_{\Delta x} \sigma_{sca}\, dx\ ,\qquad \int_{\Delta x} \sigma_{ext}\, dx\ ,\qquad \int_{\Delta x} (i_1+i_2)dx$$

where

$$\sigma_{sca}(n_{re}, n_{im}, \chi) = \frac{\lambda^2}{2\pi} \sum_{n=1}^{\infty} (2n+1) \left\{ |a_n(n_{re}, n_{im}, \chi)|^2 \right.$$

$$\left. + |b_n(n_{re}, n_{im}, \chi)|^2 \right\}$$

$$\sigma_{ext}(n_{re}, n_{im}, \chi) = \frac{\lambda^2}{2\pi} \sum_{n=1}^{\infty} (2n+1) \, \mathrm{Re} \left[ a_n(n_{re}, n_{im}, \chi) \right.$$

$$\left. + b_n(n_{re}, n_{im}, \chi) \right]$$

$$i_1(n_{re}, n_{im}, \chi, \mu) = \left| \sum_{n=1}^{\infty} \frac{2n+1}{n(n+1)} \left\{ a_n(n_{re}, n_{im}, \chi) \pi_n(\mu) \right. \right.$$

$$\left. \left. + b_n(n_{re}, n_{im}, \chi) \tau_n(\mu) \right\} \right|^2$$

$$i_2(n_{re}, n_{im}, \chi, \mu) = \left| \sum_{n=1}^{\infty} \frac{2n+1}{n(n+1)} \left\{ a_n(n_{re}, n_{im}, \chi) \tau_n(\mu) \right. \right.$$

$$\left. \left. + b_n(n_{re}, n_{im}, \chi) \pi_n(\mu) \right\} \right|^2$$

$n_{re}$ = real part, aerosol index of refraction

$n_{im}$ = imaginary part, aerosol index of refraction

$\lambda$ = wavelength

$a$ = aerosol droplet radius

$\chi = \frac{2\pi a}{\lambda}$ (size parameter)

63

$\mu = \cos$ (scattering angle)

$a_n, b_n, \pi_n, \tau_n$    are Mie-scattering functions which have been defined in a previous report[16] and the notations are standard in Mie scattering theory.

It would, of course, be desirable to construct definitive tables of $i_1 + i_2$, etc., but even rough estimates of the size of such tables show that they would be far too large to be practical with today's computer peripheral storage and access times. The present $i_1 + i_2$ tables code makes tables of the designated quantities only for fixed $n_{re}$ and $n_{im}$. Such tables have proved extremely useful in reducing the cost of Mie scattering computations for water droplet aerosols in the "visible" region of the spectrum, where $n_{re}$ and $n_{im}$ are practically constant. Even the "normal" ATRAD spectral interval structure has 44 intervals between $0.29\mu$ and $0.91\mu$ (in order to resolve the $\lambda^{-4}$ variation of Rayleigh scattering) and the cost of doing these 44 Mie calculations with re-computation of $i_1 + i_2$, etc., each time would be prohibitive. As an example of the savings to be obtained from using the $i_1 + i_2$ tables, we cite the following figures from a test calculation of the Mie tables code for a typical Arctic stratus cloud and for three spectral intervals 60-120 cm$^{-1}$, 9500-10000 cm$^{-1}$, and 20000-20500 cm$^{-1}$: without the $i_1 + i_2$ tables (which were used for the 20000-20500 cm$^{-1}$ interval only), the calculation required 292 CPU seconds on UCLA's IBM 360/91; with the $i_1 + i_2$ tables, only 65 CPU seconds were needed. Estimating that sans $i_1 + i_2$ tables, roughly 250 CPU seconds were required for the 20000-20500 cm$^{-1}$ interval, and taking this as typical for the $0.29-0.91\mu$ region (which is conservative), we see that the 44 spectral intervals in this region would require upwards of

$44 \cdot 250 = 11000$ CPU seconds (3.06 hours) of 360/91 time. These sorts of estimates point up the necessity of computational short-cuts such as the $i_1+i_2$ tables.

It should be noted that the quantities tabulated by the $i_1+i_2$ code are not $\sigma_{sca}$, $\sigma_{ext}$, and $i_1+i_2$ themsevles, but integrals of these over a small range $\Delta x$ of the size parameter. This alteration in the basic format of the code was prompted by our inability to transfer the $S^3$ version of the $i_1+i_2$ tables to UCLA without a large amount of conversion, and by the realization that the length of these tables ($i_1+i_2$ for 157 scattering angles and for $x=0.1(0.1)500$, for a total of over 785,000 words) exceeded the available disk storage at UCLA. The tables would have had to reside on tape, and consequently, runs accessing them would in all likelihood have been I/O-bound. A reconsideration of the whole matter led to the observation that $\sigma_{sca}$, $\sigma_{ext}$, and $i_1+i_2$ are all used (in the Mie tables code) in integrals of the form

$$\int_{x_{min}}^{x_{max}} (i_1+i_2) \; n(a) \; dx$$

where $n(a)$ is the aerosol size distribution. $i_1+i_2$, etc., are very rapidly varying functions of $x$, while $n(a) = n(\frac{\lambda}{2\pi}x)$ is a comparatively slowly varying function of $x$. Thus, over intervals $\Delta x$ small with respect to the scale of variation of $n(a)$, but large with respect to the scale of variation of $i_1+i_2$, we may replace $n(a)$ by some average value $\bar{n}$:

$$\int_{x}^{x+\Delta x} (i_1+i_2) \; n(a) \; dx = \bar{n}(x,\Delta x) \int_{x}^{x+\Delta x} (i_1+i_2) \; dx \quad .$$

Thus, the full integral may be approximated:

$$\int_{x_{min}}^{x_{max}} (i_1+i_2)\, n(a)\, dx = \sum_{i=1}^{N} \bar{n}(x_{min} + (i-1)\Delta x, \Delta x)$$

$$\int_{x_{min}+(i-1)\Delta x}^{x_{min}+i\Delta x} (i_1+i_2)\, dx \quad .$$

The averages $\bar{n}$ are calculated in the Mie tables code as

$$\bar{n}(x,\Delta x) = \frac{1}{\Delta x} \int_{x}^{x+\Delta x} n(a)\, dx \quad .$$

This ensures that $\bar{n}$ is a representative value for the interval $\Delta x$. Each value of $\bar{n}$ is then multiplied by the appropriate value of $\int (i_1+i_2)\, dx$ (read from the $i_1+i_2$ tables) and the sum formed. The same procedure is followed for $\sigma_{sca}$ and $\sigma_{ext}$.

A table of the "pre-integrals" $\int (i_1+i_2)\, dx$, etc., was calculated on the 360/91 for $n_{re} = 1.335$ and $n_{im} = 0$ for use in the 0.3-0.8$\mu$ spectral region for water droplet aerosols. A total of 157 scattering angles, densely distributed in the forward scattering peak region, were used, which were:

$$0°(0.1°)2°(0.2°)6°(0.5°)11°(1°)20°(2.5°)45°(5°)90°$$

plus the supplements of these angles. 500 pre-integration intervals, from (0,1) to (499,500) were taken, each of width $\Delta x = 1$. The choice $\Delta x = 1$ was based on the observation that the old $i_1+i_2$ tables were made at a 0.1 interval in $x$ and

66

that, therefore, a ten-fold reduction (from 785,000 words to 78,500 words) was possible. The variation of $n(a)$ across $\Delta x = 1$ will be small, for $\Delta x = 1$ corresponds to a radius variation of

$$\Delta a = \frac{\lambda}{2\pi}\ \Delta x = \frac{\lambda}{2\pi}\ .$$

The maximum wavelength for which these $i_1+i_2$ tables might be used is $\lambda = 0.9\mu$ , corresponding to $\Delta a = 0.14\mu$ ; and very few size distributions will vary much across any $0.14\mu$ interval. Each pre-integral was computed via the trapezoidal rule by dividing $\Delta x = 1$ up into 10 equal subintervals, thus preserving the resolution of $i_1+i_2$ , etc., down to the 0.1 scale demanded by Dave.[17] The entire table-making run consumed 1840 CPU seconds (0.51 hour) on the IBM 360/91.

In order to "page through" the $i_1+i_2$ tables and scan selected records, an interpretive program mimicing the way the Mie tables read the $i_1+i_2$ tables was constructed. This program verified the correctness of the table described in the last paragraph.

A number of changes were made in the code which calculates $\sigma_{sca}$ , $\sigma_{ext}$ , and $i_1+i_2$ . The most important change, and one particularly suited to the large core (4000K bytes) of the UCLA 360/91, is that the functions $\pi_n(\mu)$ and $\tau_n(\mu)$ are pre-computed and stored (in core) in very large arrays. This very clearly leads to economies in execution time, as opposed to re-computing $\pi_n$ and $\tau_n$ for each new value of $x$ . However, the 360/91 essentially has free core for jobs run on the graveyard shift; overall economies might not be achieved from pre-computing $\pi_n$ and $\tau_n$ on machines which charge for core. (It might be noted here that we have also experimented with keeping $\pi_n-\tau_n$ tables in peripheral storage, and that

this scheme is totally impractical given present-day access times to peripheral storage.)

Another code change involved the elimination of complex arithmetic. Complex arithmetic would be convenient for the Mie scattering calculation, since many of the quantities involved (like $a_n$ and $b_n$) are complex. However, neither the UNIVAC 1108 nor the IBM 360/91 FORTRAN compilers optimize complex operations when one of operands is real. For example, in the division of a complex by a real number, the compiler converts the real number to a complex one (by adding a zero imaginary part) and does a full complex divide, involving three floating adds, six floating multiplies, and two floating divides. If the compiler recognized the denominator as real and optimized, only two floating divides would be necessary. The Mie expressions contain many instances where real numbers are multiplied or divided with complex ones, and hence, these expressions are unsuitable for FORTRAN complex arithmetic. (Considerations such as these may seem rather esoteric to the uninitiated, but the potentially gigantic costs of Mie scattering calculations force one to examine every statement in a Mie program carefully; particular attention must be paid to avoiding re-calculating common expressions, since compilers are erratic in recognizing and storing such expressions.)

Other less substantive code changes, particularly the improvement of output formats, were also introduced. The entire code was checked out against prior calculations and found to be in agreement.

### 4.4  Mie Tables Code

This code calculates the integrals of $\sigma_{sca}$, $\sigma_{ext}$, and $i_1+i_2$ (see section 4.3) over aerosol size distribution. The integration is done using the trapezoidal rule and is both

printed and written to unformatted tables for use by ATRAD. $i_1+i_2$, etc., are either calculated in-line or read from tables, depending on the wavelength and the values of certain input variables.

A number of changes needed to be made in the Mie tables code in order to generalize it and make it a true production code, for it was the least sophisticated of the ATRAD system. It was originally split off from ATRAD and retained many features which were really irrelevant to the Mie calculation. It had a vertical zone structure mimicing ATRAD, and made a Mie scattering calculation at each atmospheric level at which aerosol was flagged as present. Thus, a Mie table was really suitable for only one particular ATRAD problem, and even such a simple change as moving the aerosol to a different level in the ATRAD calculation was non-trivial.

In order to make the Mie table as general as possible, it was necessary to allow it to generate multi-material, multi-size-distribution tables. All references to level in the atmosphere were eliminated. For each wavelength, one record is now written for each flagged material, and this record contains the polydisperse Mie scattering functions for all of the flagged size distributions for that material.

This general format for the Mie tables allows a large number of different ATRAD problems to be run from the same Mie table; ATRAD sorts through the data, taking only that for the materials and size distributions required by its internal flags. Considerable computational economy is also obtained from integrating $i_1+i_2$, etc., over many size distributions simultaneously, since the most time-consuming part of the Mie calculation is the evaluation of these mono-disperse Mie functions. Once they are evaluated, they can be multiplied by any number of size distributions and added to the trapezoidal sums with very little increase in cost over just a single size distribution.

69

As in the case of the $i_1+i_2$ tables code (see section 4.3), a large-core version of the Mie tables code was created to pre-compute and save the $\pi_n$'s and $\tau_n$'s needed for the in-line calculation of $i_1+i_2$ . This version has been checked out against prior code runs (at $S^3$) and is working satisfactorily. It is approximately 15% more efficient in terms of execution time than the code version which does not save $\pi_n$ and $\tau_n$ .

A substantial amount of effort was devoted to making the output of the Mie tables code self-explanatory and complete. The value and a detailed description of each input variable are printed out. The available analytic size distributions (Deirmendjian modified gamma, Gaussian, log-normal, and Junge power-law) are edited with descriptions of how to flag them and input their parameters. The available materials (the default set includes water, ice, soot, sea-salt, and dust) are displayed, and the tabular index of refraction of each material actually used is written out. Provision is made for inputting the name of a material not among the default materials and its tabular index of refraction as a function of wavelength, which will be linearly interpolated. If $i_1+i_2$ tables are to be used, the first records of those tables, containing identifying information, are read and the information edited. All of this furnishes a complete description of the problem setup.

Code changes had also to be made to properly process the revised form of the $i_1+i_2$ tables (which now contain $\int_{\Delta x} (i_1+i_2)\, dx$ , etc., instead of simply $i_1+i_2$ , etc.). Furthermore, the Henyey-Greenstein phase function option which was allowed in previous code versions has been eliminated. This is because it was found that replacing the real phase function by a Henyey-Greenstein approximation, even one having the same area under the forward peak, leads to erroneous flux predictions by ATRAD. The reason for this is not so much that the shape of the phase function is approximated (although the Henyey-Greenstein

phase function is poor in this respect also), but that ATRAD truncates the forward peak of the phase function if it is high enough. The truncation algorithm often produces dramatically different results for an approximating Henyey-Greenstein phase function than for the real phase function it replaces, because the algorithm is tailored to the observed behavior of realistic phase functions. And when a forward peak is truncated, the truncated fraction is assumed unscattered and the volume scattering coefficient accordingly adjusted (downwards). Thus the approximating Henyey-Greenstein phase function may lead to a scattering coefficient quite different than that calculated for the real phase function, and it is this difference which primarily leads to the large flux differences. (The Henyey-Greenstein option was first introduced in order to circumvent the impossibly long UNIVAC 1108 execution times for the Mie tables code in the visible part of the spectrum. With the advent of the $i_1+i_2$ tables, however, this problem was alleviated for water droplet aerosols. Also, the IBM 360/91, which is eight times faster than the UNIVAC 1108, has brought all execution times more within reason.)

Some experiments were made at selected wavelengths ($125\mu$, $1\mu$, and $0.49\mu$) for the Arctic stratus size distribution[7] to determine how conservative the various parameters controlling the trapezoidal integration over size distribution must be. Two important facts were discovered:

(1) the observation of Dave[17] that an integration increment of $\Delta x = 0.1$ is sufficient was confirmed (using $\Delta x = 0.05$ led to only slight changes in the results);

(2) another observation of Dave's[18], that the integration increment $\Delta x$ could be increased to $5\Delta x$ after a large fraction of the aerosol particles (99%) had been integrated over, was proven wrong; it was necessary to use a

71

larger fraction, 99.9%, in order to obtain accurate results, and with a fraction this close to 100% little if any computational savings are realized.

The second result is not meant to impugn the work of Dave, but merely to point up that his method of "telescoping" the integration increment is not general since it did not work for the Arctic stratus size distribution.

We offer a final retrospective observation on methods of performing the integration over size distribution. Over almost four years we have experimented with a number of schemes to shorten the computation time for this integration. These schemes ranged from the sophisticated, such as the Henyey-Greenstein replacement (discussed above) or the Romberg extrapolation-to-the-limit of multiple trapezoidal quadratures, down the gamut to the simple, such as variants of Dave's telescoping integration increment and stopping the ingration when the maximum relative change in the trapezoidal sums in one integration step was small enough. All of these schemes saved computer time, but all of them broke down and produced inaccurate results in one situation or another. No general scheme for saving a substantial amount of computer time and still producing guaranteed accurate results has been found to supplant the simple trapezoidal integration from $x_{min}$ to $x_{max}$ with a step size

$$\Delta x = \min \left( 0.1, \frac{x_{max} - x_{min}}{200} \right) .$$

## 4.5 ATRAD — Code Improvements

A large number of improvements have been made in ATRAD since the previous report on this contract.[7] Among the changes which have been introduced are:

(1) a facility for looping over multiple values of sun angle, surface albedo, surface temperature, or "top" temperature;

(2) options for specular reflection and for ascribing a temperature and emissivity to the top level in the mesh (corresponding, say, to a cirrus cloud);

(3) greater efficiency in the Grant-Hunt algorithm coding, in particular a cessation of calculations (when thermal emission is negligible) below the level at which sunlight falls to a negligible value on account of absorption (applicable to near-IR and UV spectral intervals);

(4) the editing of a detailed description of each input variable, so that ATRAD is virtually self-explanatory in terms of I/O;

(5) an enormous expansion of the available options for inputting atmospheric vertical structure;

(6) new logic for reading the new generalized type of Mie tables, for editing descriptive information from the ID record of those tables, for skipping through unwanted sections of the tables, and for processing the desired tabular data into the correct atmospheric levels;

(7) allowing spectral-interval-by-spectral-interval flux edits at up to four "slices" through the vertical mesh, thus alleviating the necessity for taking the full flux edits at all levels in order to extract such information;

(8)  allowing input of tabular surface albedos (diffuse
and specular) as functions of wavelength, to be
linearly interpolated to obtain albedos in each
spectral interval; the only alternative albedo
option, a user-supplied subroutine (for more
sophisticated effects such as angular dependence),
has been liberally supplied with comments to
assist the user; and,

(9)  making edits more intelligible to the unfamiliar
user, and supplying units information with all
quantities edited.

Item (1), looping over multiple parameters, would be
trivial if it simply involved multiple executions of the entire
code.  However, when a parameter such as sun angle varies, many
of the most time-consuming parts of ATRAD are not affected.
Thus what was actually done was to loop only over those sec-
tions of code involving the parameter in question.  The savings
to be achieved by doing this are exemplified by the following
figures:  for one sun angle, a full clear sky ATRAD execution
(from 60 to 48500 $cm^{-1}$) requires about 40 CPU seconds on the
IBM 360/91; for ten sun angles, this figure only jumps to 113
CPU seconds, less than a three-fold increase.

As for the atmospheric vertical structure (item (5)),
the categories now available are:

(a)  a Mintz-Arakawa 2-level atmosphere, calculated
from temperature, humidity, etc. furnished for some subset of
$\sigma = 0, 1/4, 1/2, 3/4, 1$;

(b)  a standard tropical, midlatitude (summer or winter),
or subarctic (summer or winter) atmosphere;

(c)   a user-supplied atmosphere, for which the sub-options
are:

(i)   to supply only altitude levels or pressure
levels; the missing variable will be calculated from
the hydrostatic approximation taking account of
humidity and the vertical variation of gravity;

(ii)   to supply either water vapor mixing ratio
or water vapor density; the missing variable will be
calculated; and

(iii)   to flag an analytic exponential-in-altitude
or power-law-in-pressure mixing ratio profile, with
parameters supplied by the user,

For both the Mintz-Arakawa and user-supplied atmospheres, there
are options to:

(a)   flag an analytic ozone profile, with user-input
parameters, and

(b)   flag an exponentially-decreasing-in-altitude
aerosol number density, also with user-input parameters.

For the standard atmospheres, the options are for the user to
input his own altitude mesh (which generates an interpolated
standard atmosphere), to input his own aerosol structure, and
to scale the standard humidity and ozone profiles by constant
(input) factors.

### 4.6   ATRAD — Code Runs

ATRAD is operational on the UCLA IBM 360/91 and has been
delivered to the Rand Climate Dynamics Group.  Numerous ATRAD
runs have been and are being made for Rand to demonstrate ATRAD
and its capabilities.

All ATRAD runs to be described below were made for the standard tropical atmosphere of McClatchey, et.al.,[19] for the spectral region 60-48500 cm$^{-1}$ and for ten sun angles $\theta_{sun}$ such that $\cos\theta_{sun}$ = 0.1, 0.2, ..., 1.0.

The first pair of calculations which were examined were identical in all respects except that one used exponential fitting tables generated some time ago at S$^3$ on the UNIVAC 1108 and the other used exponential fitting tables generated only recently at UCLA on the IBM 360/91. These two tables were substantially different because (a) the fitting is sensitive to differences in machine precision, and (b) the method of choosing transmission data to be fitted had been changed (see section 4.2). Nevertheless, the total fluxes predicted in the two runs never differed by more than 6 w/m$^2$ out of 1000 w/m$^2$, or 0.6%. The heating rates between reasonably widely-spaced levels never differed by more than 0.1 degrees/day. Thus, the insensitivity of the flux predictions to substantial variations in the exponential fitting parameters is demonstrated.

The second pair of calculations to be compared were one using the "normal" ATRAD spectral interval structure and one using the much more refined structure (in cm$^{-1}$)

60(20)2400(100)11000(200)32000(500)48500

As discussed in section 4.2, a second exponential fitting table was made for this refined structure on the 360/91. Because of the large number of spectral intervals in the refined calculation (119 in the IR, 4-125μ; 84 in the near-IR, 0.91-4μ; and 138 in the "visible" and UV 0.21-0.91μ) this calculation was broken up into three sections, one for the IR, one for the near-IR, and one for the "visible" and UV. For the IR part of the spectrum, the fluxes for the "normal" and refined spectral

76

interval structures agreed at all vertical levels to within $\pm 0.3$ watts/$m^2$. For the near-IR, they agreed to within anywhere from $\pm 0.1$ watts/$m^2$ at $\cos\theta_{sun} = 0.1$ to $\pm 1.5$ watts/$m^2$ at $\cos\theta_{sun} = 1.0$. For the "visible" and UV, they agreed to within anywhere from $\pm 0.1$ watts/$m^2$ for $\cos\theta_{sun} = 0.1$ to $\pm 0.3$ watts/$m^2$ for $\cos\theta_{sun} = 1.0$. Thus, the "normal" ATRAD spectral interval structure proves to be spectrally refined enough to satisfy the model's assumption that the Planck function, scattering and continuum absorption coefficients, scattering phase function, and solar flux do not vary significantly across a spectral interval (or else, if they do vary substantially, it is across spectral intervals which contribute negligibly to the flux).

The extreme variation of $\pm 1.5$ watts/$m^2$ in the near-IR for a zenith sun deserves some further discussion. It is our feeling that this difference, small as it is (it is only 1/2% of the flux in question), is too large to be due solely to the spectral resolution. We feel that the bulk of the difference is due rather to the inadequacy of the exponential fitting algorithm in the strong near-IR $H_2O$ bands. As explained in section 4.2, that algorithm is simply unable to take sufficiently many points to resolve the transmission curve in strong bands. When the spectral interval structure is more refined, that problem is more localized (in the band centers) and thus has less impact on the total flux. In the future, a more sensible ATRAD spectral interval structure would take very fine steps (perhaps even as small as 20 $cm^{-1}$) across the centers of these strong bands, with much larger steps elsewhere. In fact, this measure had already been taken in the "normal" ATRAD spectral interval structure across the 15μ $CO_2$ band (20 $cm^{-1}$ steps) because early in the development of the code it was found that unacceptable flux errors were incurred when 60 $cm^{-1}$ steps were taken.

The problem discussed in the last paragraph has less impact in the IR region, in spite of the strong $H_2O$ bands there,

because in those very bands where the largest errors might be incurred, the net fluxes are smallest due to the near-equality of up- and down-fluxes.

A series of ATRAD runs have also been made for a wide range of surface albedos (all the runs discussed above had a zero surface albedo). These will be used to create a table showing the dependence of the Earth-atmosphere albedo on sun angle and surface albedo.

## 4.7 Future Work

Several tasks will be completed by the close of the contract. These are:

(1) the creation of a Mie scattering table for water for a variety of aerosol size distributions;

(2) the execution of ATRAD for one or two problems using the Mie table in (1);

(3) delivering the following items to Rand --

   (a) exponential fitting code

   (b) exponential fitting tables ("normal" and refined)

   (c) $i_1+i_2$ tables code

   (d) $i_1+i_2$ table

   (e) Mie tables code

   (f) Mie table

   (g) rational function fitting code

   (h) listings and, in the case of codes, sample executions of items (a) — (g);

(4) instructing Rand personnel in use of all delivered codes;

78

(5)   complete work on fitting atmospheric solar absorption with rational functions of the absorber amount; and,

(6)   write a summary of the exponential fitting algorithm.

REFERENCES

1.  Pretherton, F.P., "Momentum Transport by Gravity Waves," Quarterly J.R. Met. Soc. (April, 1969), Vol. 95.

2.  Bretherton, F.P., "The Propagation of Groups of Internal Gravity Waves in a Shear Flow," Quarterly J.R. Met. Soc. (1966), Vol. 92.

3.  Bretherton, F.P. and J.R. Booker, "The Critical Layer for Internal Gravity Waves in a Shear Flow," J. Fluid Mech. (March, 1967, Vol. 27.

4.  Quency, P., "The Problem of Air Flow Over Mountains: A Summary of Theoretical Studies," Bull. Amer. Meteor. Soc. (Jan., 1948), Vol. 29.

5.  Scorer, R.S., "Theory of Waves in the Lee of Mountains," Quart. J.R. Met. Soc. (1949), Vol. 75, p. 41.

6.  Phillips, O.M., The Dynamics of the Upper Ocean, Cambridge University Press, 1966, pp. 178-185.

7.  "The Effects of Meso-Scale and Small-Scale Interactions on Global Climate," Report No. SSS-R-73-1727, Contract No. DAHC04-73-C-0003 (June 15, 1973), Systems, Science and Software, La Jolla, California.

8.  "The Effects of Meso-Scale and Small-Scale Interactions on Global Climate," Report No. SSS-R-74-2023, Contract No. DAHC04-73-C-0003 (Jan. 7, 1974), Systems, Science and Software, La Jolla, California.

9.  Palm, E. and A. Foldvik, "Contribution to the Theory of Two-Dimensional Mountain Waves," Geofys. Publ. (June, 1960), Vol. 21.

10. Vergeiner, I., "An Operational Linear Lee Wave Model," Quart. J.R. Met. Soc. (1971), Vol. 97.

11. Weather Tapes Obtained from the National Weather Service, Ashville, N.C.

## REFERENCES (continued)

12. Crutcher, H.L., "Meridional Cross Sections - Upper Winds Over the Northern Hemisphere," U.S. Dept. of Commerce Tech. Paper No. 41 (June, 1961).

13. Klemp, J.B. and D.K. Lilly, Submitted to J. Atm. Sci. (May, 1974).

14. Selby, J.E.A. and R. McClatchey, "Atmospheric Transmittance from 0.25 to 28.5 μm: Computer Code LOWTRAN 2," Report AFCRL-72-0745, Air Force Cambridge Research Labs, Bedford, Mass. (Dec., 1972).

15. Thekaekara, M., "Solar Energy Outside the Earth's Atmosphere," Solar Energy 14, 109-127 (1973).

16. Freeman, B., W. Wiscombe, and W. England, "The Effects of Meso-Scale and Small-Scale Interactions on Global Climate," Semi-Annual Technical Report for Period 15 Feb. 1972 through 14 Aug. 1972, Report No. SSS-R-72-1255, Systems, Science and Software, La Jolla, California (Sept., 1972).

17. Dave, J., "Effect of Coarseness of the Integration Increment on the Calculation of the Radiation Scattered by Polydispersed Aerosols," Appl. Opt. 8, 1161 (1969).

18. Dave, J., "Effect of Varying Integration Increment on the Calculation of Radiation Scattered by Polydispersed Aerosols," Appl. Opt. 8, 2153 (1969).

19. McClatchey, R., et. al., "Optical Properties of the Atmosphere," Report AFCRL-70-0527, Air Force Cambridge Research Labs, Bedford, Mass. (1970).